# Supplementary Information

## Reconstructing interfacial electric double layer for efficient sulfur conversion reaction in aqueous zinc sulfur batteries

Jie Lei[1,2], Jiandong Lin[1,2], Yinze Zuo[1,2,*], Yong Yan[1,2], Yue Lu[1,2], Rongxin Gao[1,2], Peining Lin[1,2], Mingquan Liu[1,2], Hao Yan[1,2], Wei Yan[1,2,*] & Jiujun Zhang[1,2,*]

[1] Institute for New Energy Materials and Engineering, College of Materials Science and Engineering, Fuzhou University, Fuzhou 350108, China.

[2] Fujian Engineering Research Center of High Energy Batteries and New Energy Equipment & Systems, Fuzhou 350108, China.

**E−mail**: yinzezuo@fzu.edu.cn; weiyan@fzu.edu.cn; jiujun.zhang@fzu.edu.cn

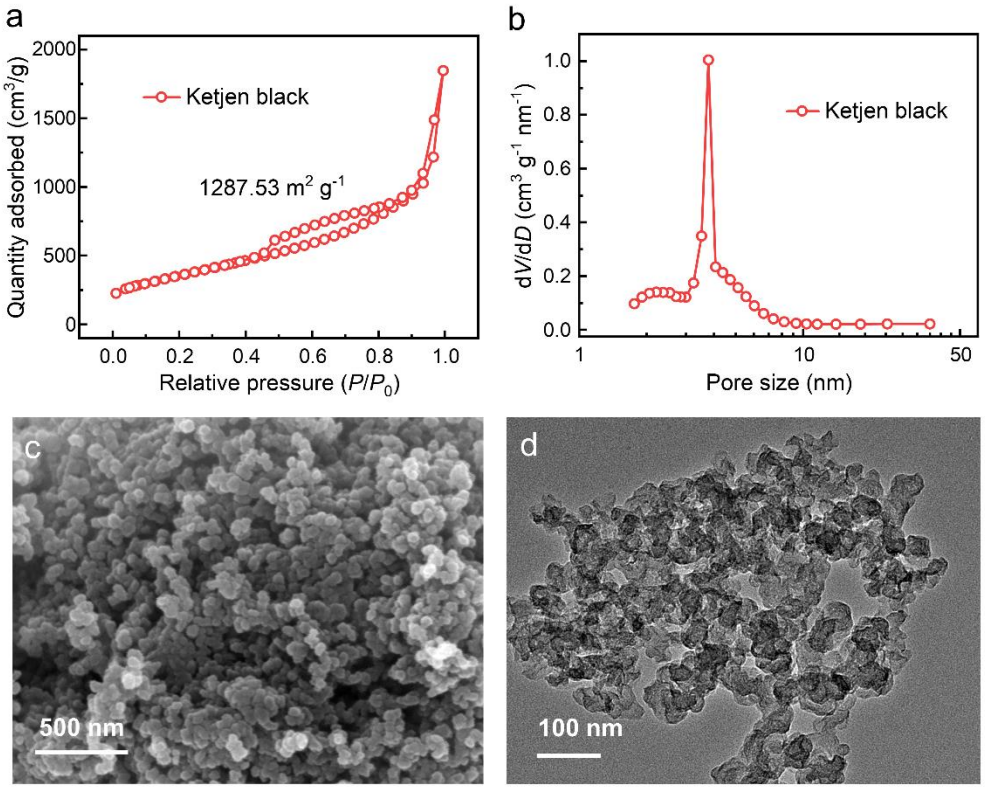


**Supplementary Fig. 1 | The physical characterization of Ketjen black (KB).** (a) $N_2$ adsorption–desorption isotherm loop. (b) Pore–size distribution plot. (c) SEM image and (d) TEM image of KB material.

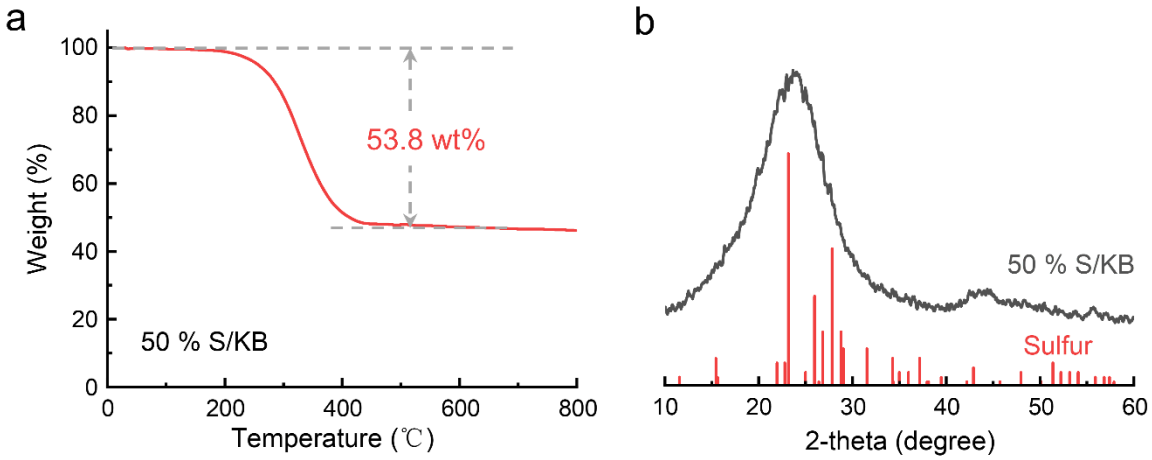


**Supplementary Fig. 2 | The physical characterization of sulfur/Ketjen black (S/KB) composites.** (a) Thermogravimetric analysis and (b) XRD pattern of S/KB composites.

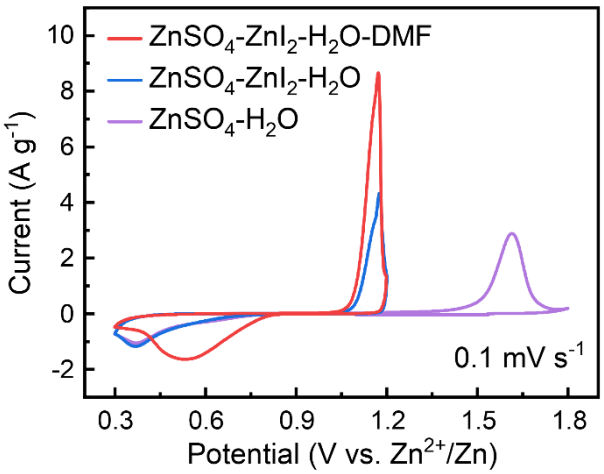


**Supplementary Fig. 3**|CV Profiles of Zn||S cells with $ZnSO_4$–$H_2O$, $ZnSO_4$–$ZnI_2$–$H_2O$, and $ZnSO_4$–$ZnI_2$–$H_2O$–DMF electrolytes at a scan rate of 0.1 mV $s^{-1}$.

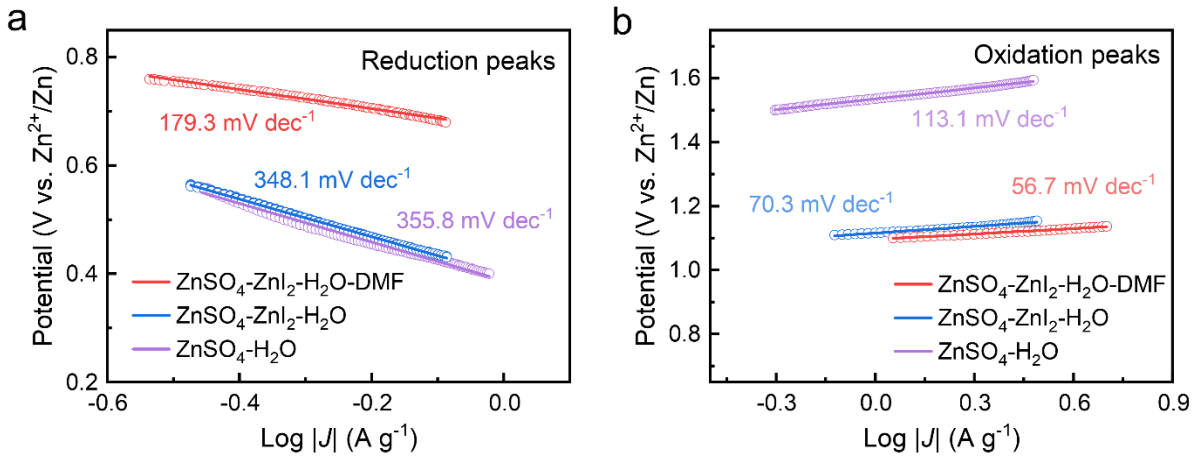


**Supplementary Fig. 4** | Tafel plots calculated from (a) reduction peaks and (b) oxidation peaks.

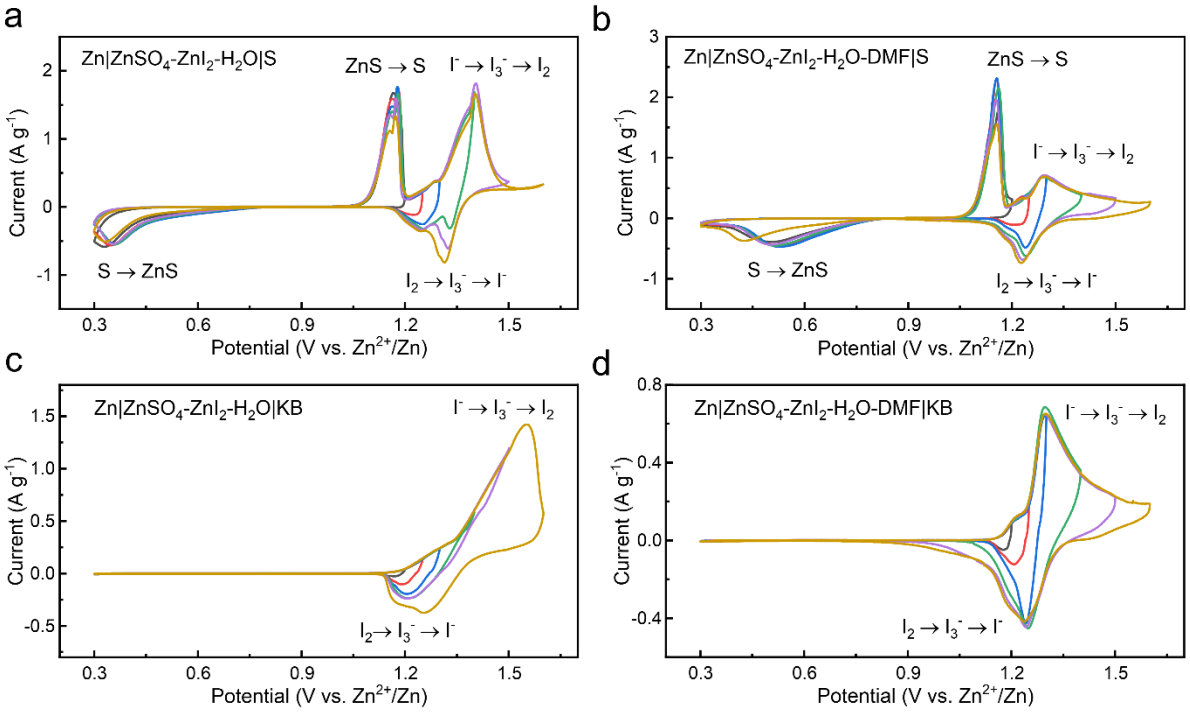


**Supplementary Fig. 5** | (a, b) CV profiles of S/KB electrode in $ZnSO_4$−$ZnI_2$−$H_2O$, and $ZnSO_4$−$ZnI_2$−$H_2O$−DMF electrolytes. (c, d) CV profiles of sulfur–free KB electrode in $ZnSO_4$−$ZnI_2$−$H_2O$, and $ZnSO_4$−$ZnI_2$−$H_2O$−DMF electrolytes.

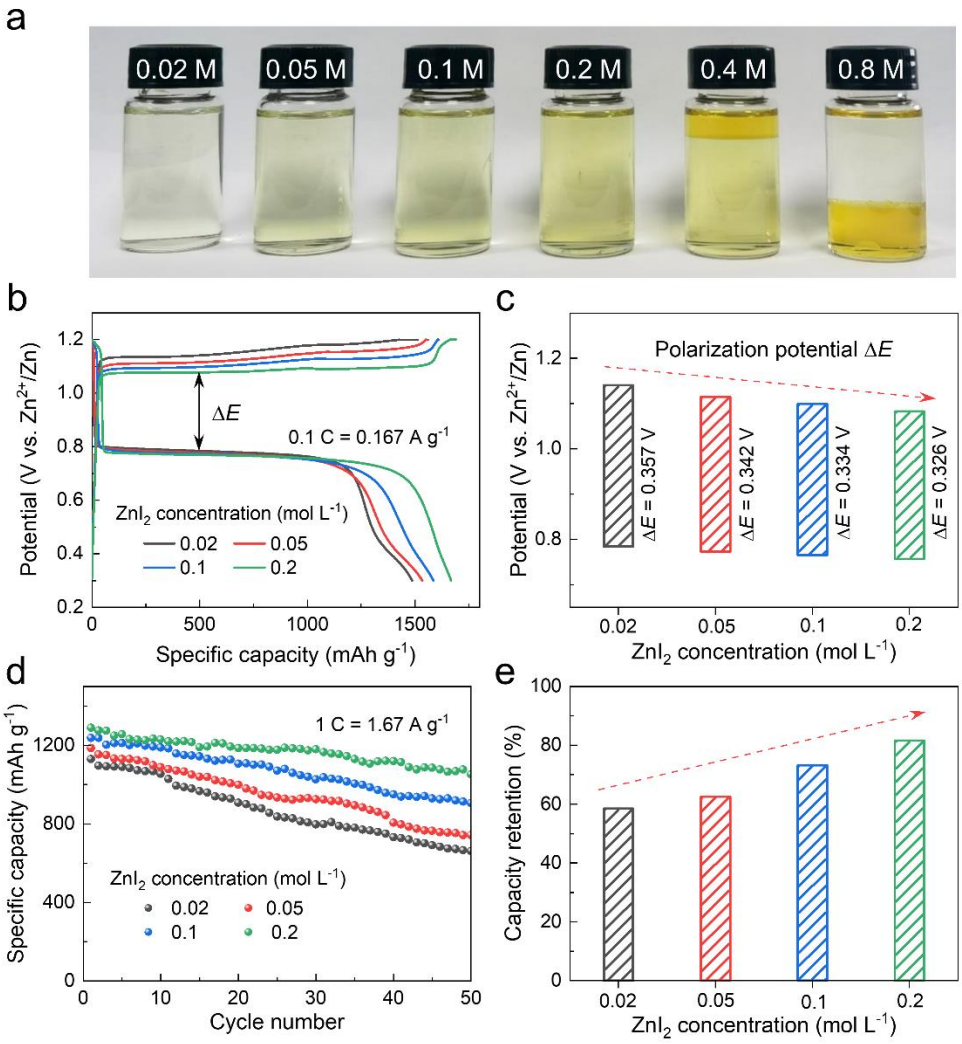


**Supplementary Fig. 6**|(a) The optical photographs of hybrid electrolytes with different $ZnI_2$ concentrations. (b) The fifth–cycle galvanostatic charge–discharge curves of the Zn||S cells. (c) Polarization potentials obtained from (b). (d) cycling performance of the Zn||S cells. (e) Capacity retention obtained from (d).

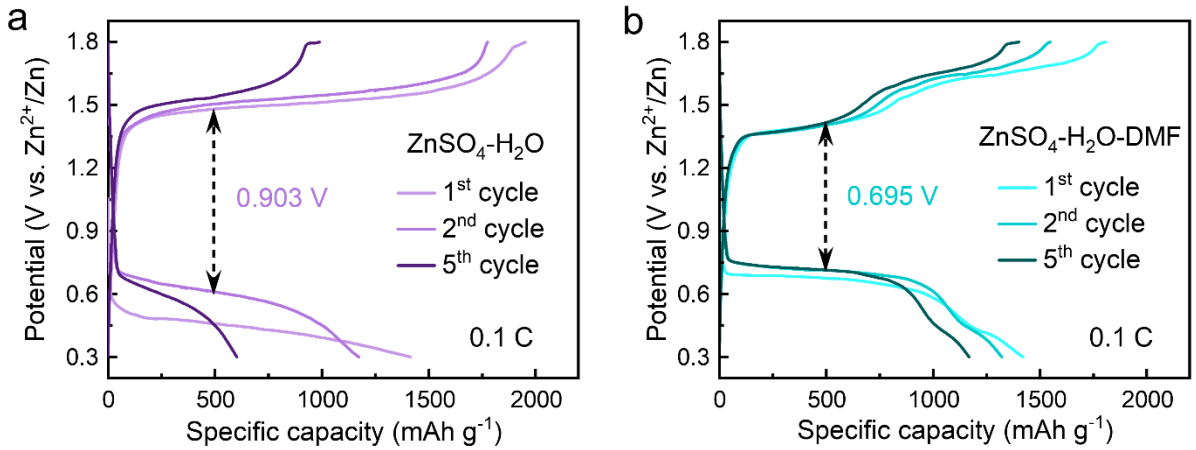


**Supplementary Fig. 7** | Galvanostatic charge–discharge curves of the Zn||S cells with (a) $ZnSO_4$−$H_2O$ and (b) $ZnSO_4$−$H_2O$−DMF electrolytes at 0.1 C.

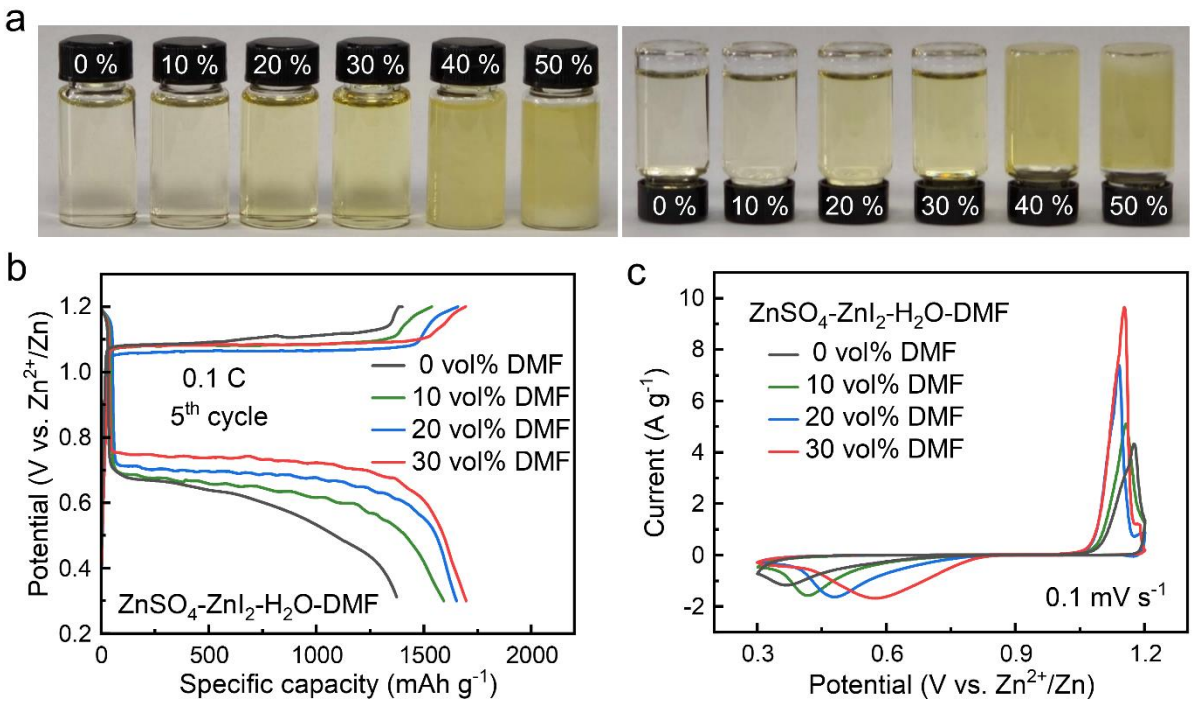


**Supplementary Fig. 8** | (a) The optical photographs of hybrid electrolytes with different volume concentrations of DMF. (b) The fifth–cycle galvanostatic charge–discharge curves and (c) the corresponding CV profiles of the Zn||S cells in the $ZnSO_4$–$ZnI_2$–$H_2O$ electrolytes with different concentration of DMF.

**Note:** Although the DMF concentration exceeding 30 vol% could be achieved by reducing the concentration of zinc salts, this also results in decreased ionic conductivity, negatively affecting high–rate performance of Zn||S batteries for high–power–density practical applications. Besides, while not a scientific drawback, higher DMF concentration would increase cost and may raise handling/safety concerns due to its toxicity. Based on the overall consideration, the optimized volume concentration of DMF is identified to be 30 vol% in this work.

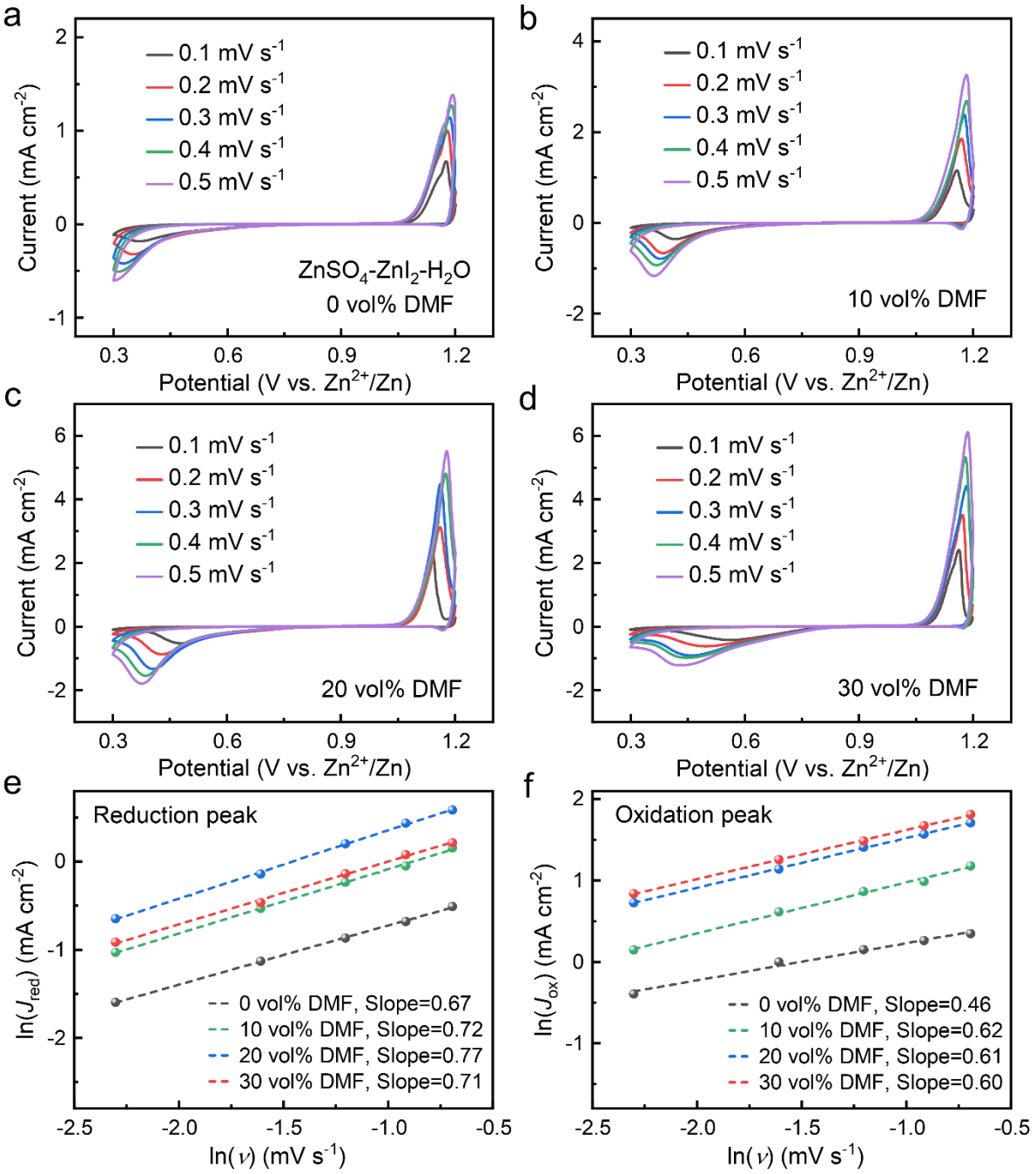


**Supplementary Fig. 9**|(a–d) CV profiles of the Zn||S cells under different scan rates from 0.1 to 0.5 mV $s^{-1}$ in the $ZnSO_4$–$ZnI_2$–$H_2O$ electrolytes with different concentration of DMF. (e, f) Proportional relation between the reduction/oxidation peak current density and scan rate in logarithmic plots.

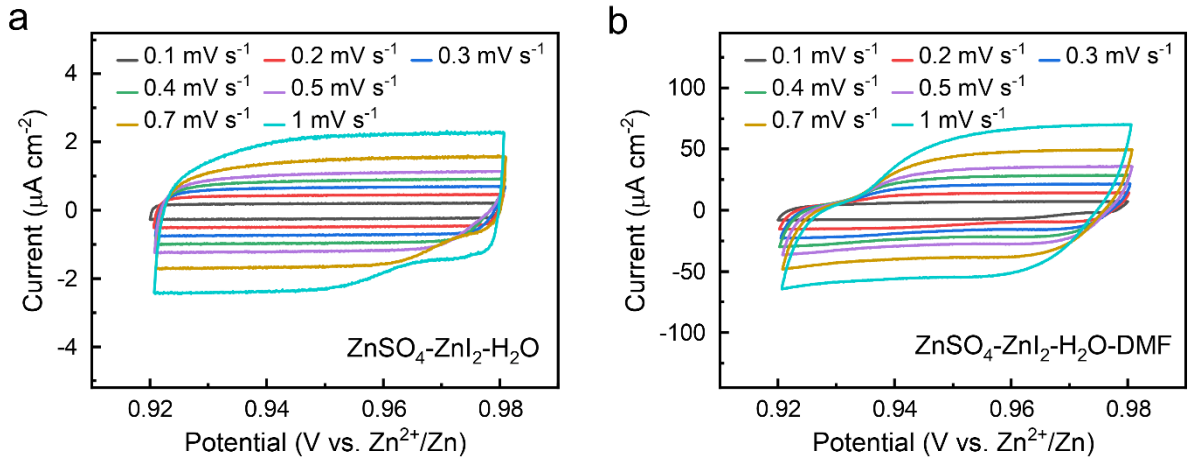


**Supplementary Fig. 10**|CV profiles of the Zn||S cells in the potential range between 0.92 V and 0.98 V (vs. $Zn^{2+}/Zn$) with (a) $ZnSO_4$–$ZnI_2$–$H_2O$ and (b) $ZnSO_4$–$ZnI_2$–$H_2O$–DMF electrolytes.

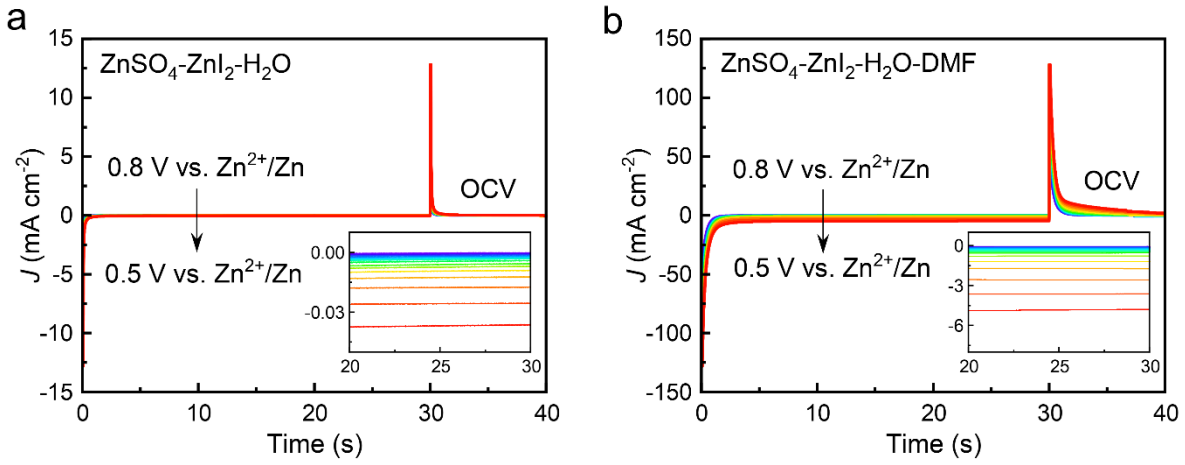


**Supplementary Fig. 11** | Pluse current response during the reductive potenital−OCP step from the pulse voltammetry protocol of Zn||S cells with (a) $ZnSO_4$−$ZnI_2$−$H_2O$ and (b) $ZnSO_4$−$ZnI_2$−$H_2O$−DMF electrolytes.

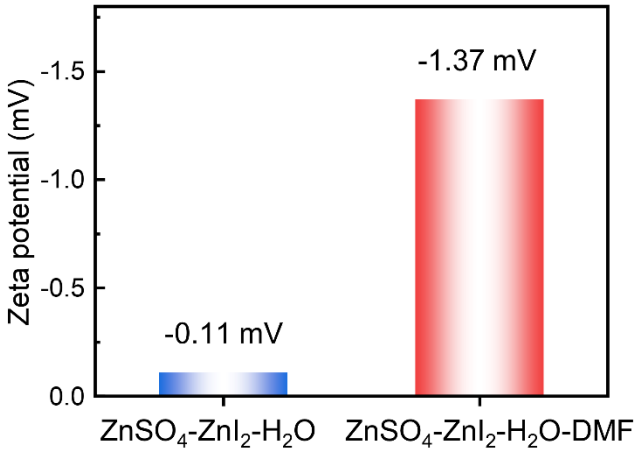


**Supplementary Fig. 12**|Zeta potential of the sulfur electrode in the $ZnSO_4$−$ZnI_2$−$H_2O$ and $ZnSO_4$−$ZnI_2$−$H_2O$−DMF electrolytes.

**Note:** Zeta potentials of sulfur electrodes in different electrolytes were measured to experimentally disclose the surface charge states. As presented in Supplementary Fig. 12, the sulfur electrode in the $ZnSO_4$−$ZnI_2$−$H_2O$−DMF electrolye shows a lower Zeta potential of −1.37 mV compared with that of −0.11 mV in the $ZnSO_4$−$ZnI_2$−$H_2O$ electrolye, signifying that much more negative charges are adsorbed at the electrode interface.

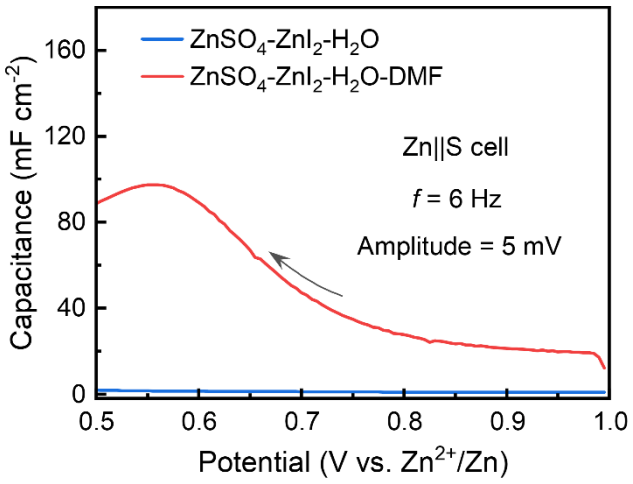


**Supplementary Fig. 13**|The alternating current (A.C.) voltammetry measurement for Zn||S cells with $ZnSO_4$−$ZnI_2$−$H_2O$ and $ZnSO_4$−$ZnI_2$−$H_2O$−DMF electrolytes.

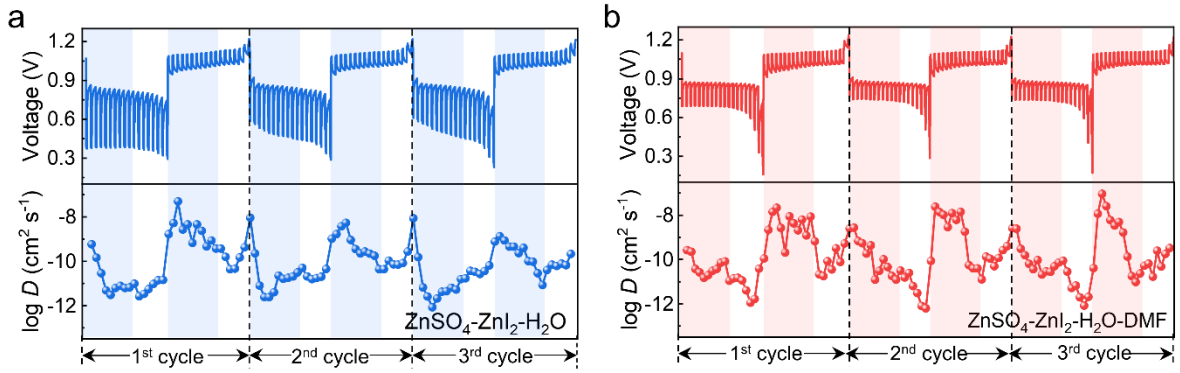


**Supplementary Fig. 14**| The GITT voltage profiles and Zn–ion diffusion coefficients of sulfur electrode in the (a) $ZnSO_4$–$ZnI_2$–$H_2O$ and (b) $ZnSO_4$–$ZnI_2$–$H_2O$–DMF electrolytes.

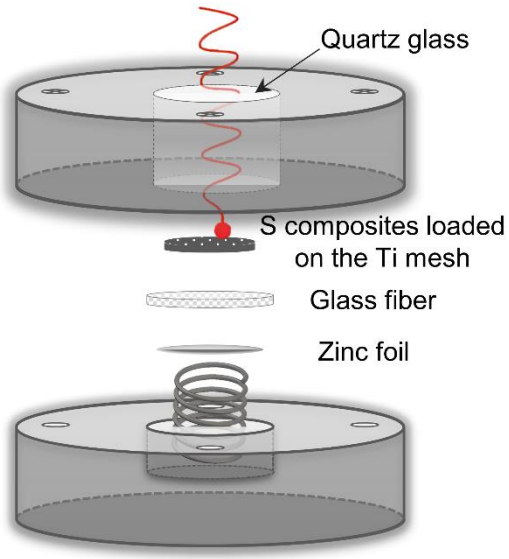


**Supplementary Fig. 15**| Schematic diagram of Operando Raman cell configuration.

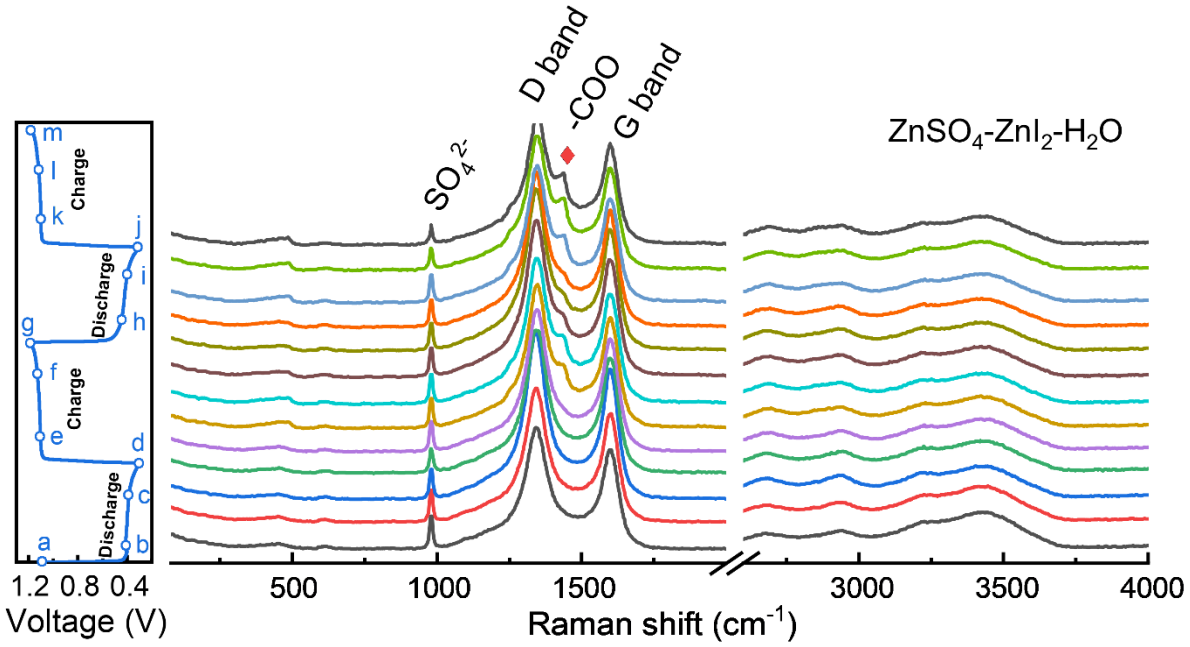


**Supplementary Fig. 16 |** Operando Raman spectra of sulfur electrode surface during the discharge−charge process in the $ZnSO_4$−$ZnI_2$−$H_2O$ electrolyte.

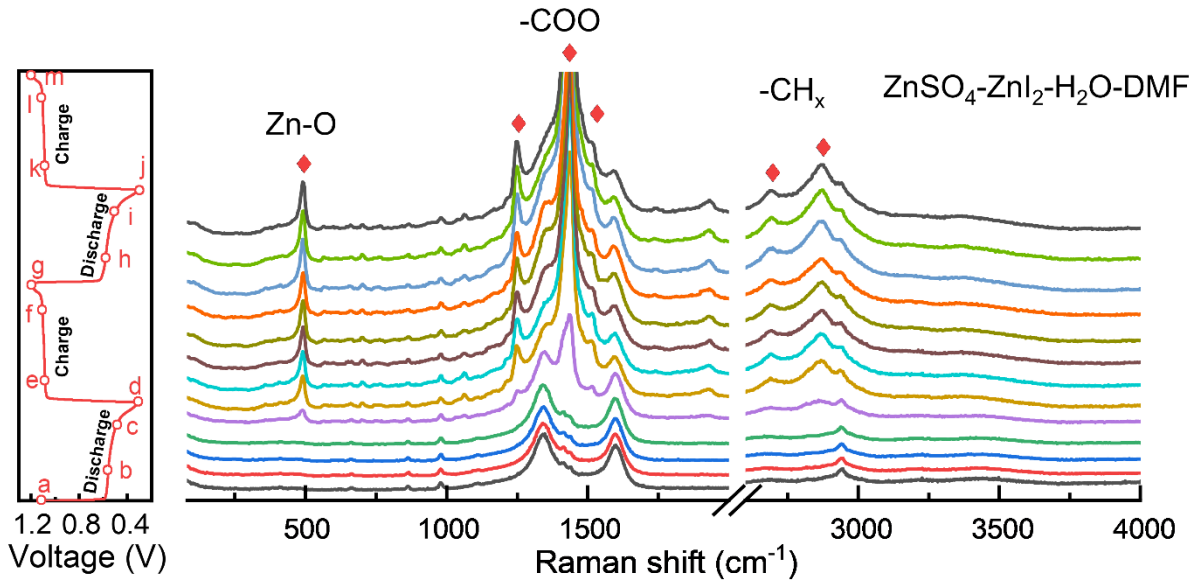


**Supplementary Fig. 17 |** Operando Raman spectra of sulfur electrode surface during the discharge−charge process in the $ZnSO_4$−$ZnI_2$−$H_2O$−DMF electrolyte.

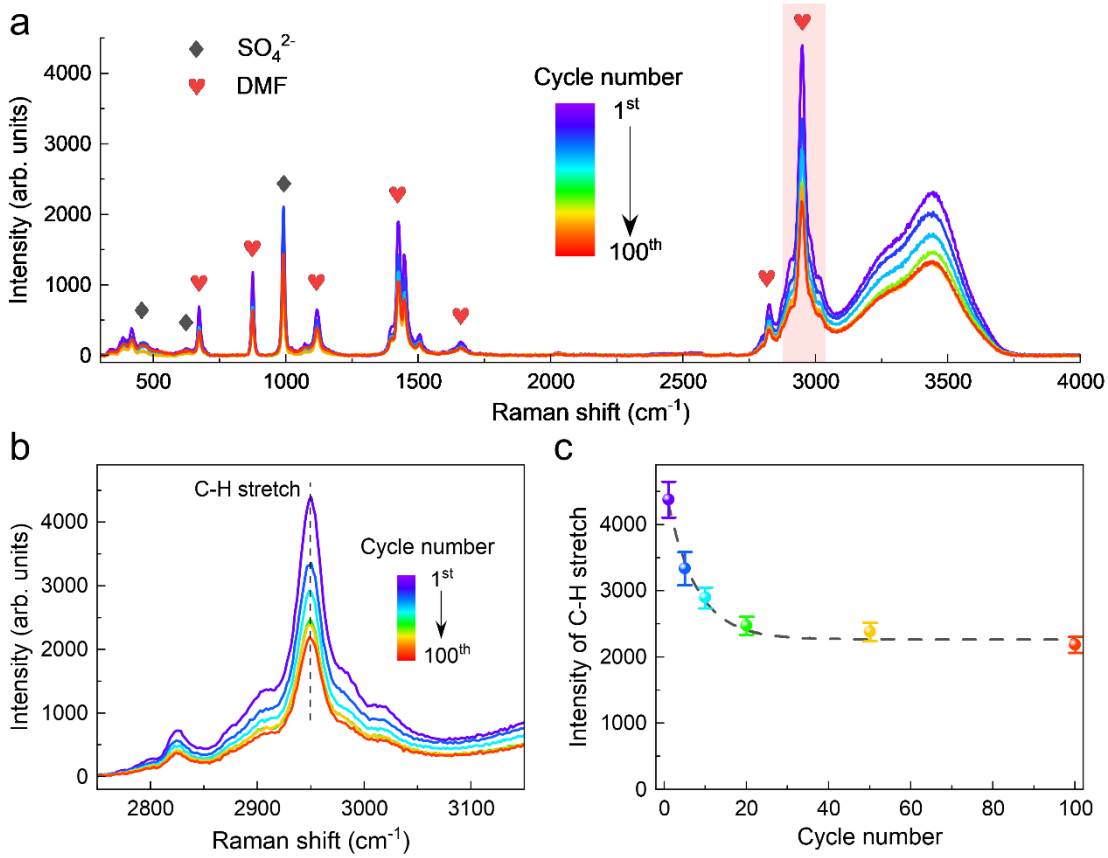


**Supplementary Fig. 18**|(a) Raman spectra of the wetted separators from the disassembled Zn||S cells after different cycles (1, 5, 10, 20, 50, 100 cycles at 1 C). (b) Enlarged view of (a) representing the C−H stretching of DMF. (c) Intensity change of Raman peak corresponding to the C−H stretching of DMF during the initial 100 cycles.

**Note:** In order to investigate the consumption of DMF during the cycle process, the Zn||S batteries after different cycles (1, 5, 10, 20, 50, 100 cycles at 1 C) were disassembled, and the Raman spectra of the wetted separators were immediately acquired to prevent the evaporation of electrolyte solvent. The experimental errors can be reduced as much as possible through respectively disassembling at least three identical cells at the same conditions. As shown in Supplementary Fig. 18, the characteristic Raman peaks of DMF could still be observed after 100 cycles. As a representative, the C–H stretching of DMF located at 2950 $cm^{-1}$ is selected to determine the DMF concentration via the peak intensity, which shows a continuous decline during the initial 20 cycles, but keeps unchanged in the subsequent battery cycles. This indicates that the oxidative decomposition of DMF would hardly occur after the initial 20 cycles, thus ensuring the electrolyte stability in the long–term cycling process of Zn||S battery.

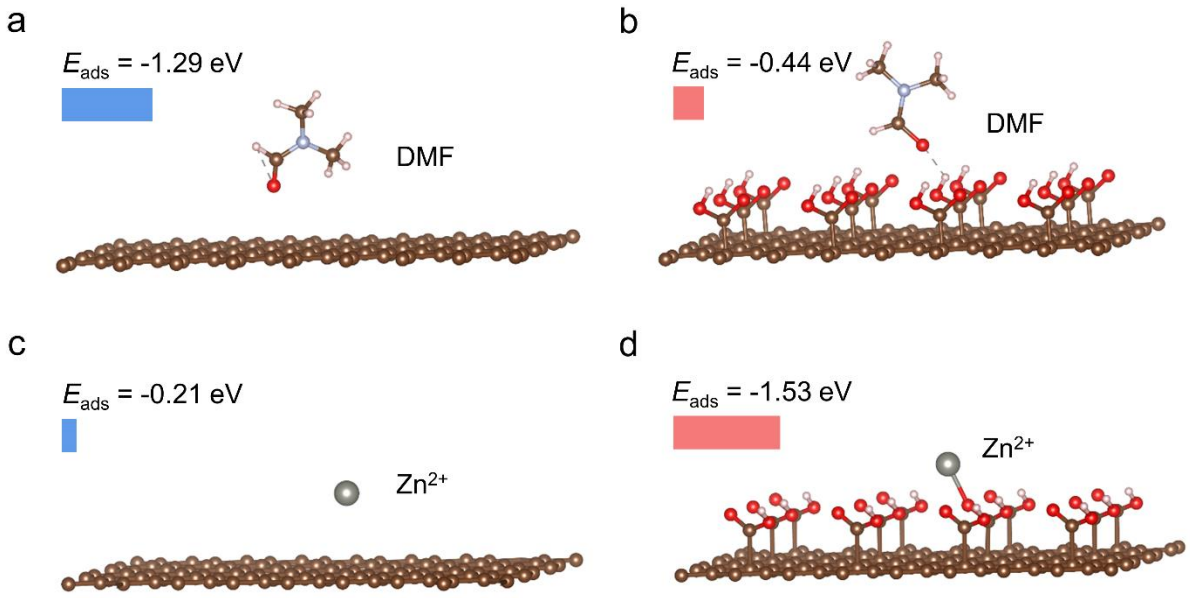


**Supplementary Fig. 19**| Calculated adsorption energies of (a, b) DMF and (c, d) $Zn^{2+}$ on the carbon substrates without and with rich carboxyl groups.

**Note:** As resulted in Supplementary Fig. 19, the –COO groups as decomposition products of DMF, could inhibit the surface adsorption of DMF, while enhance the $Zn^{2+}$ adsorption on the sulfur electrode, which have been proved by the theoretical calculations of adsorption energies. This can well explain the suppressed DMF decomposition after the initial 20 cycles of Zn||S batteries mentioned above. Moreover, –COO groups would be functionalized as a substitute of DMF for $Zn^{2+}$ enrichment at the sulfur electrode interface to accelerate sulfur conversion reaction in the long-term cycling process.

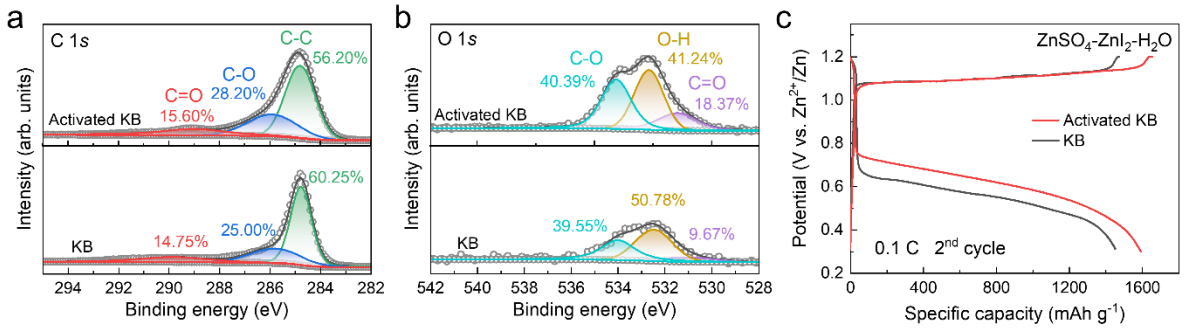


**Supplementary Fig. 20**|XPS profiles of (a) C 1*s* and (b) O 1*s* peaks for pristine KB and activated KB materials. (c) Galvanostatic charge−discharge curves of Zn||S cells with $ZnSO_4$−$H_2O$−DMF electrolytes at 0.1 C.

**Note:** Activated the Ketjen black (KB) with surface partial oxidation was prepared through a simple hydrothermal method (the detailed synthesis process is as follows). The chemical composition of activated KB material was characterized using the X−ray photoelectron spectroscopy (XPS). As shown in Supplementary Fig. 20a, the XPS spectra of C 1*s* can be separated into three deconvoluted peaks located at 289.2 eV, 285.9 eV and 284.8 eV, which are ascribed to the C=O, C–O and C–C bonds on the surface of carbon materials, respectively. Compared with the pristine KB, the activated KB displays stronger C=O and C–O signals, indicating more oxygen–containing functional groups on the surface. This also can be confirmed by the XPS spectra of O 1*s*, in which activated KB exhibits an obviously higher intensity response than pristine KB (Supplementary Fig. 20b). Subsequently, the sulfur composites and sulfur electrode were prepared through the similar method, except using the activated KB instead of KB. Zn||S cells were assembled with the $ZnSO_4$−$ZnI_2$−$H_2O$ electrolyte without DMF cosolvent. As shown from the galvanostatic charge−discharge (GCD) curves in Supplementary Fig. 20c, the sulfur/activate KB composite performs a significantly reduced reaction polarization for the discharging process. All the above results evidently demonstrate that the carboxyl group could play the same role as DMF, to some extent, to enrich $Zn^{2+}$ on the electrode surface to accelerate sulfur reduction reaction.

**Synthesis of activated Ketjen black (KB):** Typically, 200 mg of the commercial KB was uniformly dispersed in a mixed solvent (100 mL) of $H_2O$ and DMF with the volume ratio of 7:3. The resulted black solution was then sealed in a Teflon–lined stainless–steel autoclave and maintained at 160 ℃ for 2 hours. After cooling down, the activated KB material can be fabricated by washing with deionized water for several times and subsequent freeze–drying.

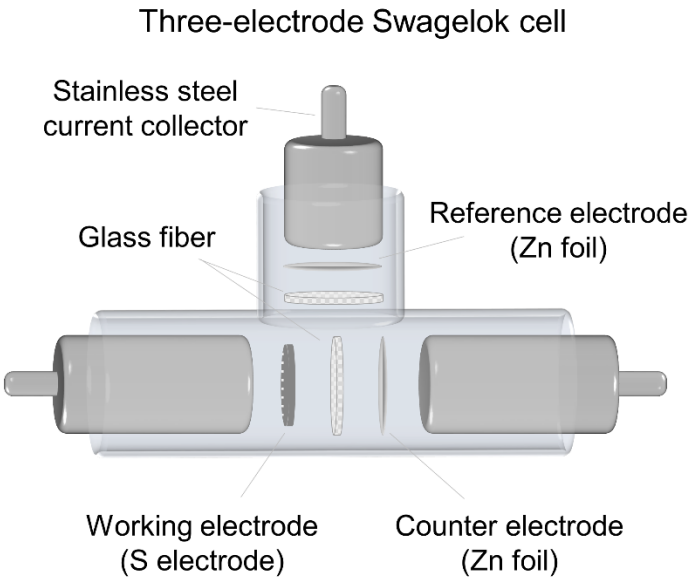


**Supplementary Fig. 21**| Schematic diagram of a three−electrode Swagelok cell configuration for *in situ* EIS tests.

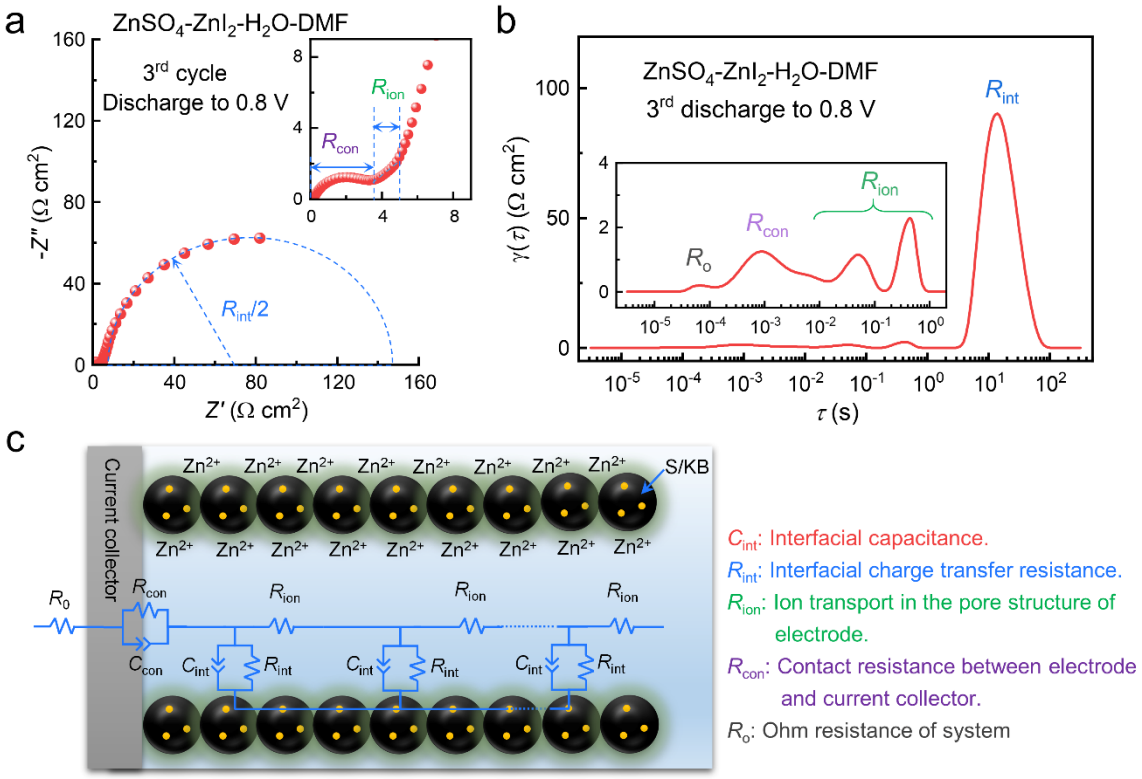


**Supplementary Fig. 22**|(a) Nyquist plot and (b) corresponding DRT spectra of the Zn||S cell with $ZnSO_4$–$ZnI_2$–$H_2O$–DMF electrolyte after discharging to 0.8 V in the third cycle. The inserted figures are the partially enlarged images of high–frequency region. (c) Scheme of the underlying electrochemical processes in the porous sulfur electrode and the affiliated impedance elements according to the transmission line model.

Note: To elucidate the underlying physical mechanisms governing the impedance arcs of porous sulfur electrode in the Zn||S cell with $ZnSO_4$–$ZnI_2$–$H_2O$–DMF electrolyte, the Nyquist plot upon discharging to 0.8 V in the third cycle was taken as an example. As shown in Supplementary Fig. 22a, the resistance value of low-frequency impedance arc is much higher than that of high-frequency impedance arc. According to the transmission line model (TLM) of porous electrodes, the relaxation time ($\tau$) identifications of different electrochemical processes during sulfur conversion reaction can be conducted. As shown Supplementary Fig. 22b, the high–frequency impedance arc ($10^{-4}$ s < $\tau$ <$10^{-2}$ s) should be attributed to the contact resistance between the electrode and the current collector ($R_{con}$). The presence of non–vertical line in the mid–frequency region ($10^{-2}$ s < $\tau$ <1 s) generally represents the ion transport in the pore structure of electrode ($R_{ion}$). And the low–frequency arc (1 s < $\tau$ <$10^{2}$ s) can be interpreted as the interfacial charge transfer resistance ($R_{int}$), which is demonstrated to be the largest and dominates the kinetics of sulfur conversion reactions. The corresponding equivalent circuit diagram is presented in Supplementary Fig. 22c.

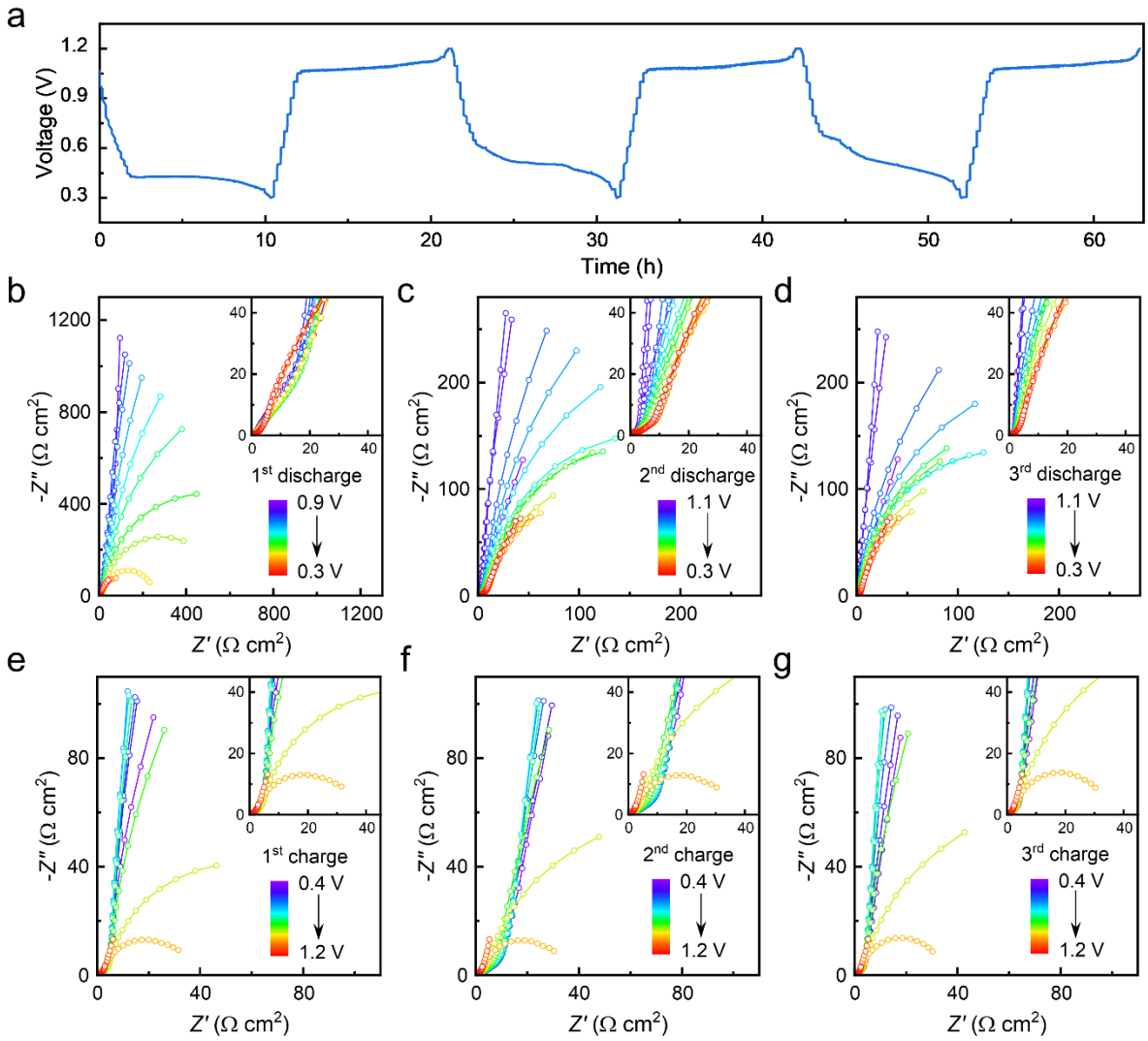


**Supplementary Fig. 23 | *In situ* GEIS measurements of sulfur electrode at different potentials with $ZnSO_4$–$ZnI_2$–$H_2O$ electrolyte.** (a) Potential profiles and (b–g) Potential–dependent impedance spectra in the initial three cycling process. The insets are the partially enlarged images of high–frequency region.

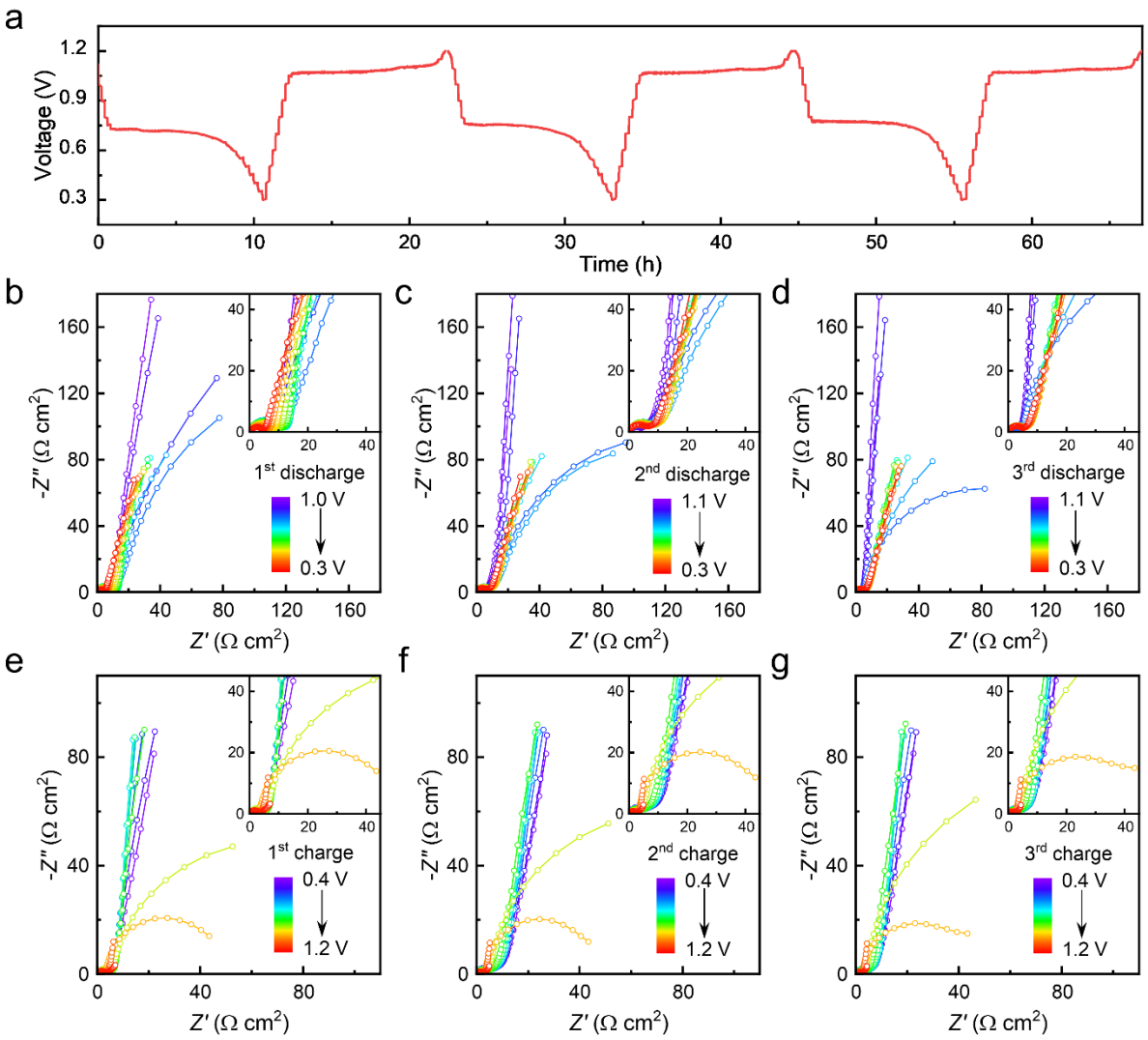


**Supplementary Fig. 24 | *In situ* GEIS measurements of sulfur electrode at different potentials with $ZnSO_4$–$ZnI_2$–$H_2O$–DMF electrolyte.** (a) Potential profiles and (b–g) Potential−dependent impedance spectra in the initial three cycling process. The insets are the partially enlarged images of high–frequency region.

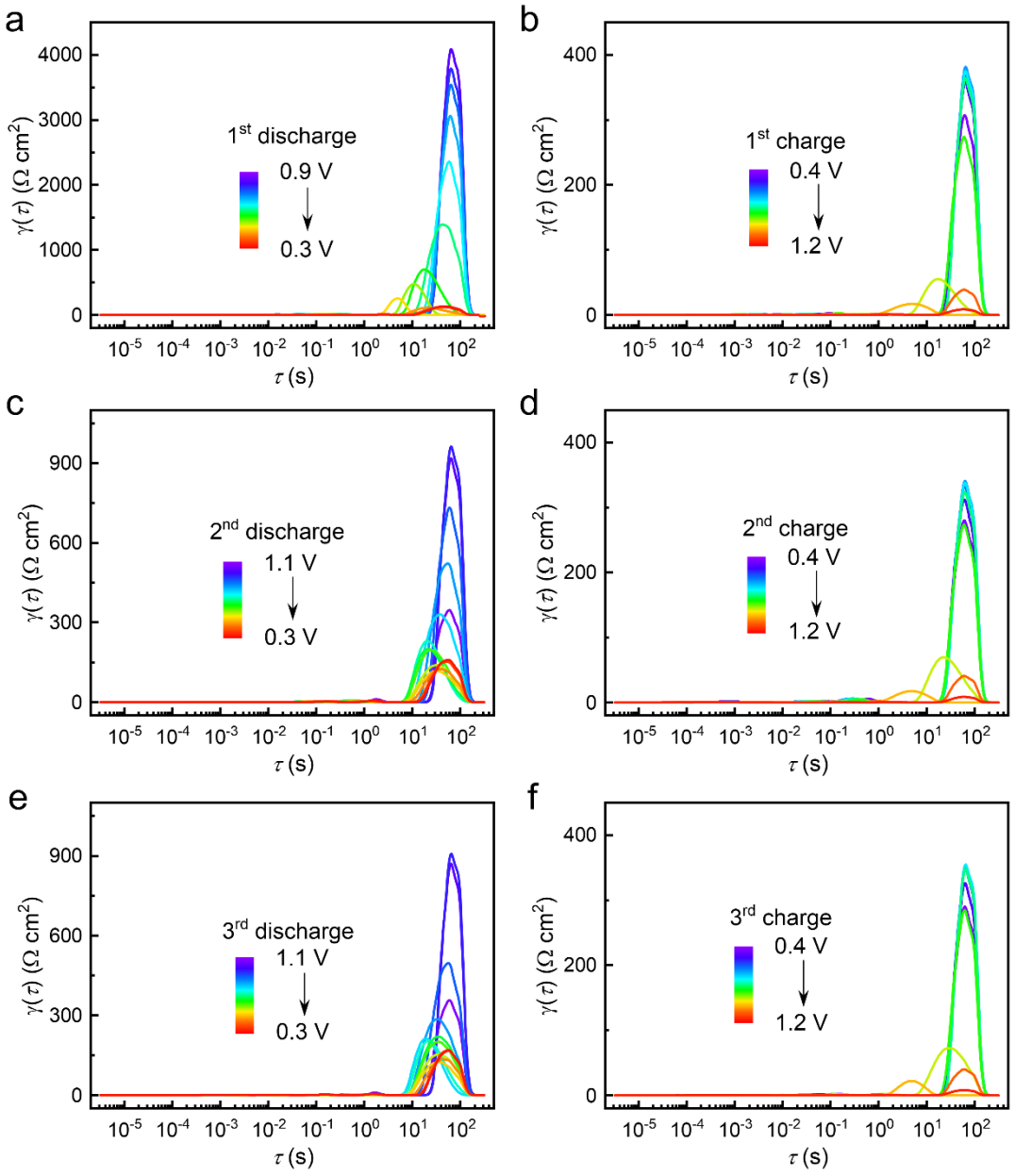


**Supplementary Fig. 25**|DRT analysis of potential−dependent impedance spectra obtained from *in situ* GEIS measurements of sulfur electrode with $ZnSO_4$−$ZnI_2$−$H_2O$ electrolyte in the (a) 1st−cycle discharging, (b) 1st−cycle charging, (c) 2nd−cycle discharging, (d) 2nd−cycle charging, (e) 3rd−cycle discharging, (f) 3rd−cycle charging processes.

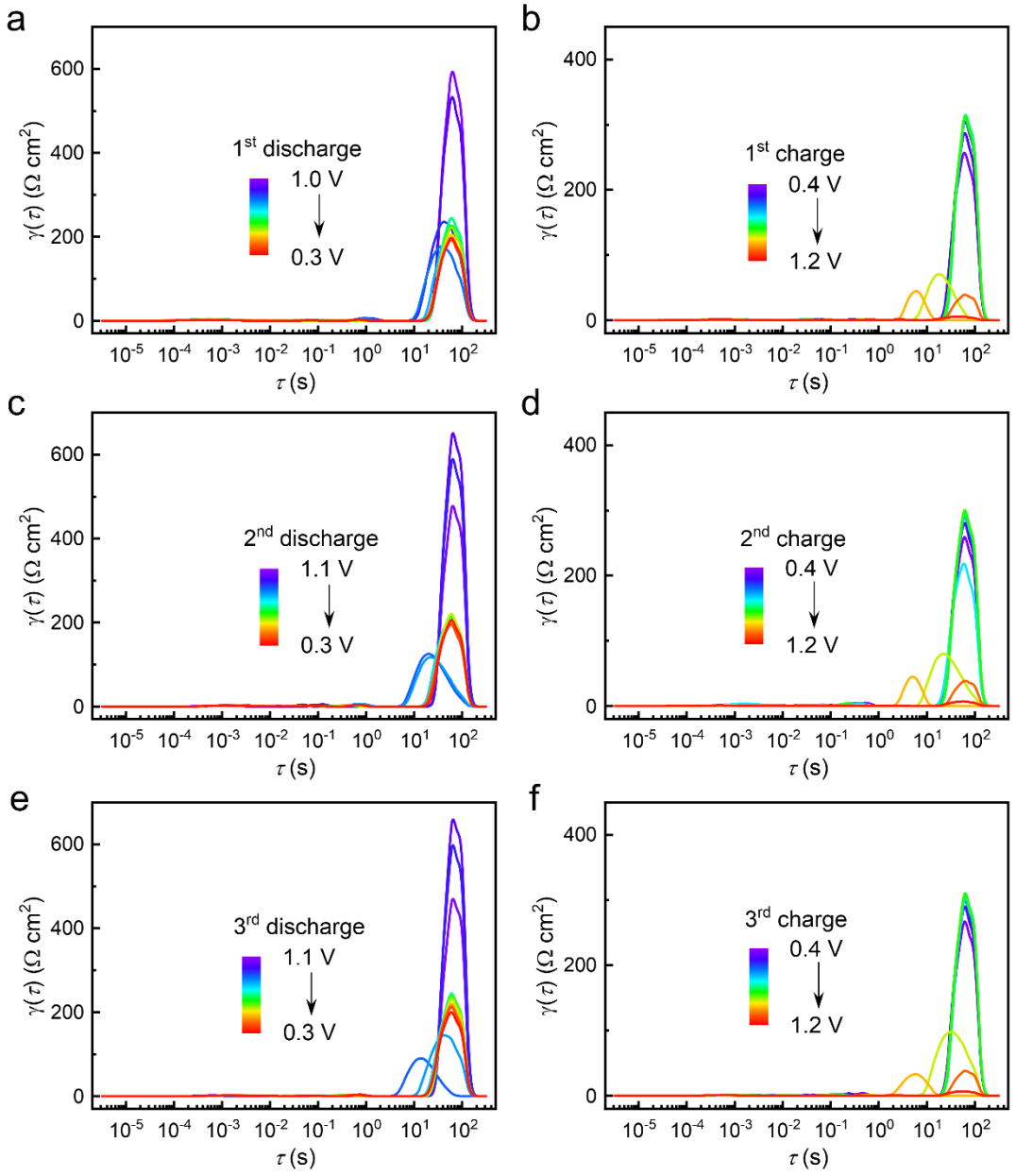


**Supplementary Fig. 26**|DRT analysis of potential−dependent impedance spectra obtained from *in situ* GEIS measurements of sulfur electrode with $ZnSO_4$−$ZnI_2$−$H_2O$−DMF electrolyte in the (a) 1st−cycle discharging, (b) 1st−cycle charging, (c) 2nd−cycle discharging, (d) 2nd−cycle charging, (e) 3rd−cycle discharging, (f) 3rd−cycle charging processes.

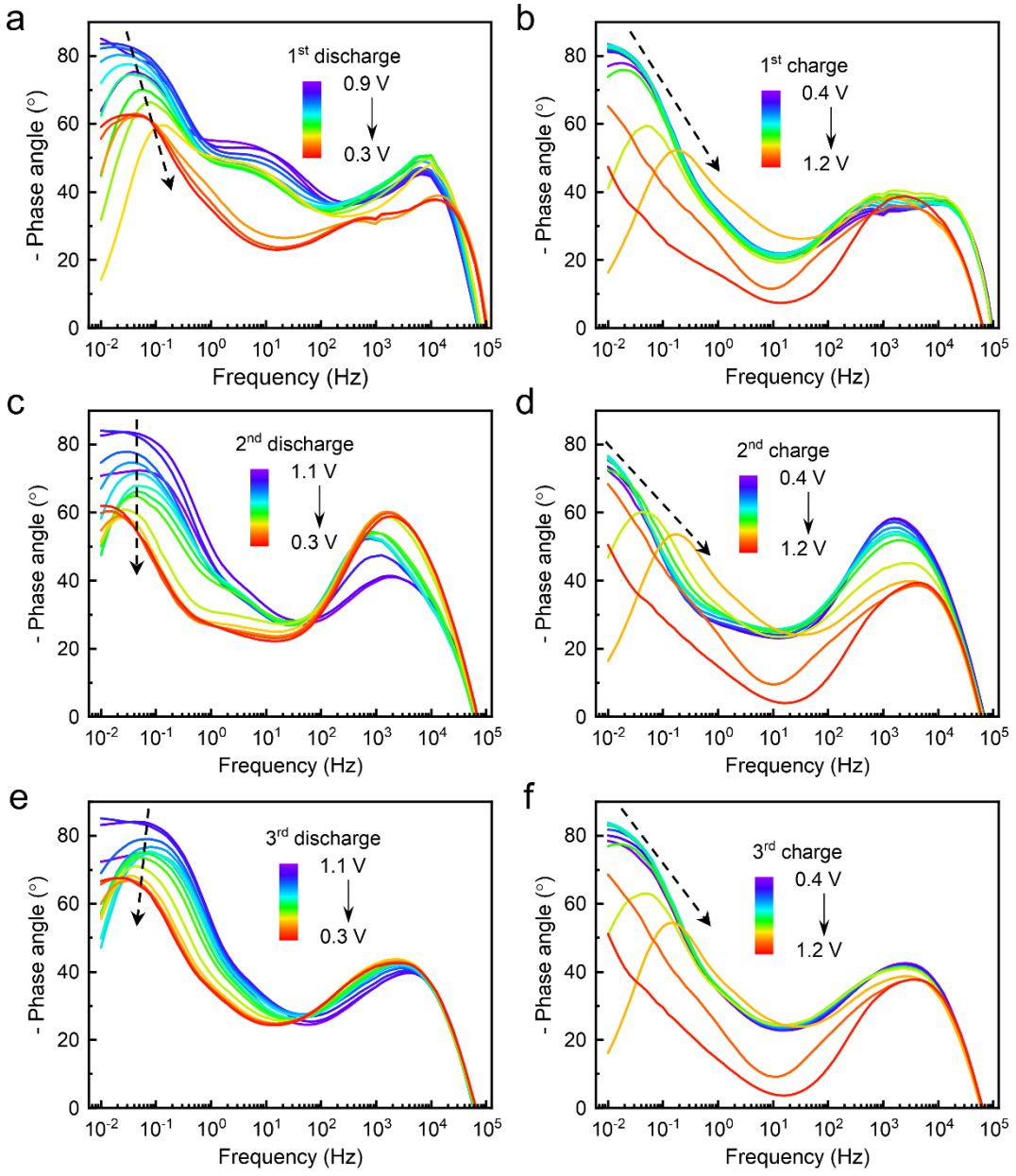


**Supplementary Fig. 27**|Bode plots of potential−dependent impedance spectra obtained from *in situ* GEIS measurements of sulfur electrode with $ZnSO_4$−$ZnI_2$−$H_2O$ electrolyte in the (a) 1st−cycle discharging, (b) 1st−cycle charging, (c) 2nd−cycle discharging, (d) 2nd−cycle charging, (e) 3rd−cycle discharging, (f) 3rd−cycle charging processes.

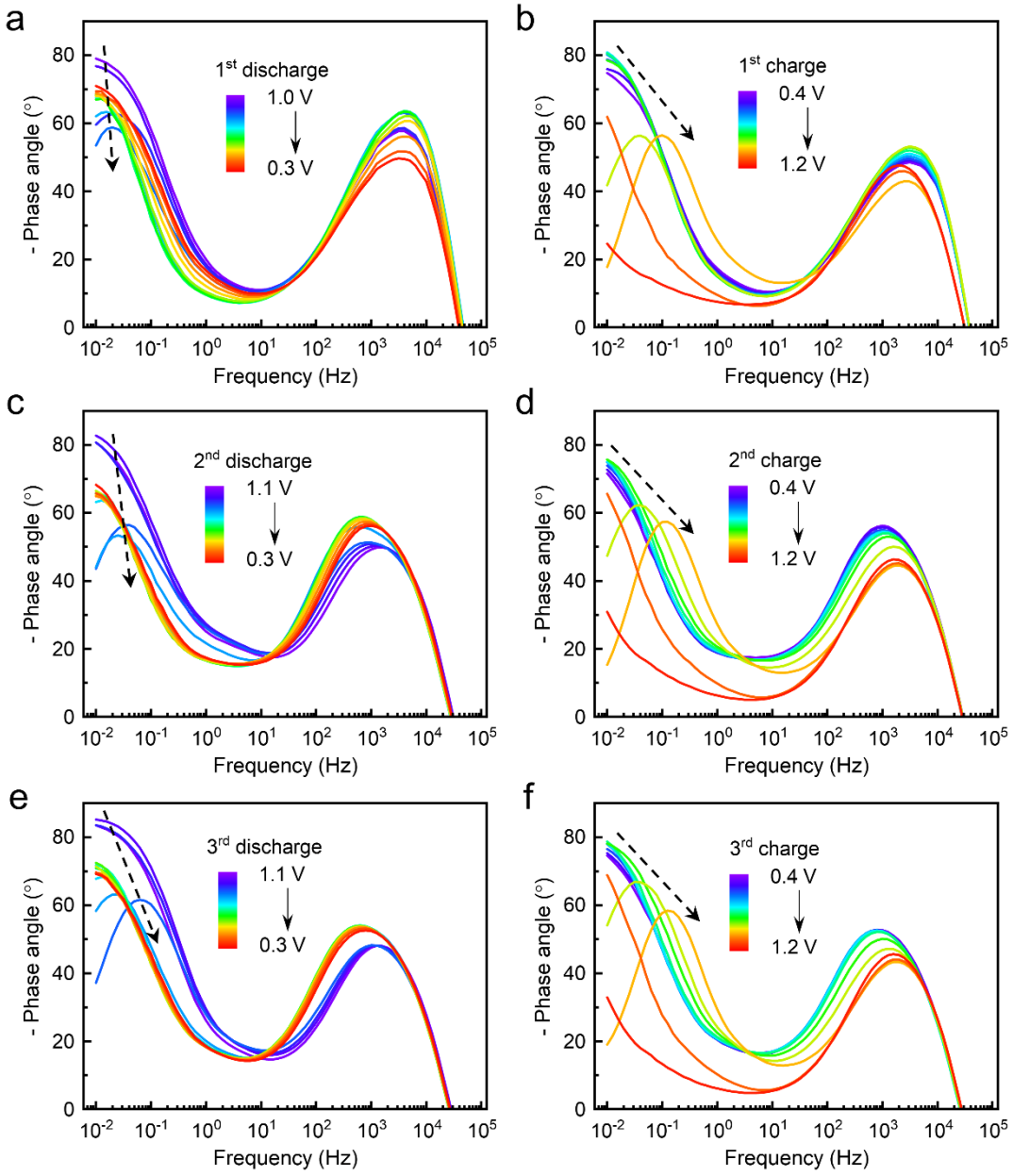


**Supplementary Fig. 28**| Bode plots of potential−dependent impedance spectra obtained from *in situ* GEIS measurements of sulfur electrode with $ZnSO_4$−$ZnI_2$−$H_2O$−DMF electrolyte in the (a) 1st−cycle discharging, (b) 1st−cycle charging, (c) 2nd−cycle discharging, (d) 2nd−cycle charging, (e) 3rd−cycle discharging, (f) 3rd−cycle charging processes.

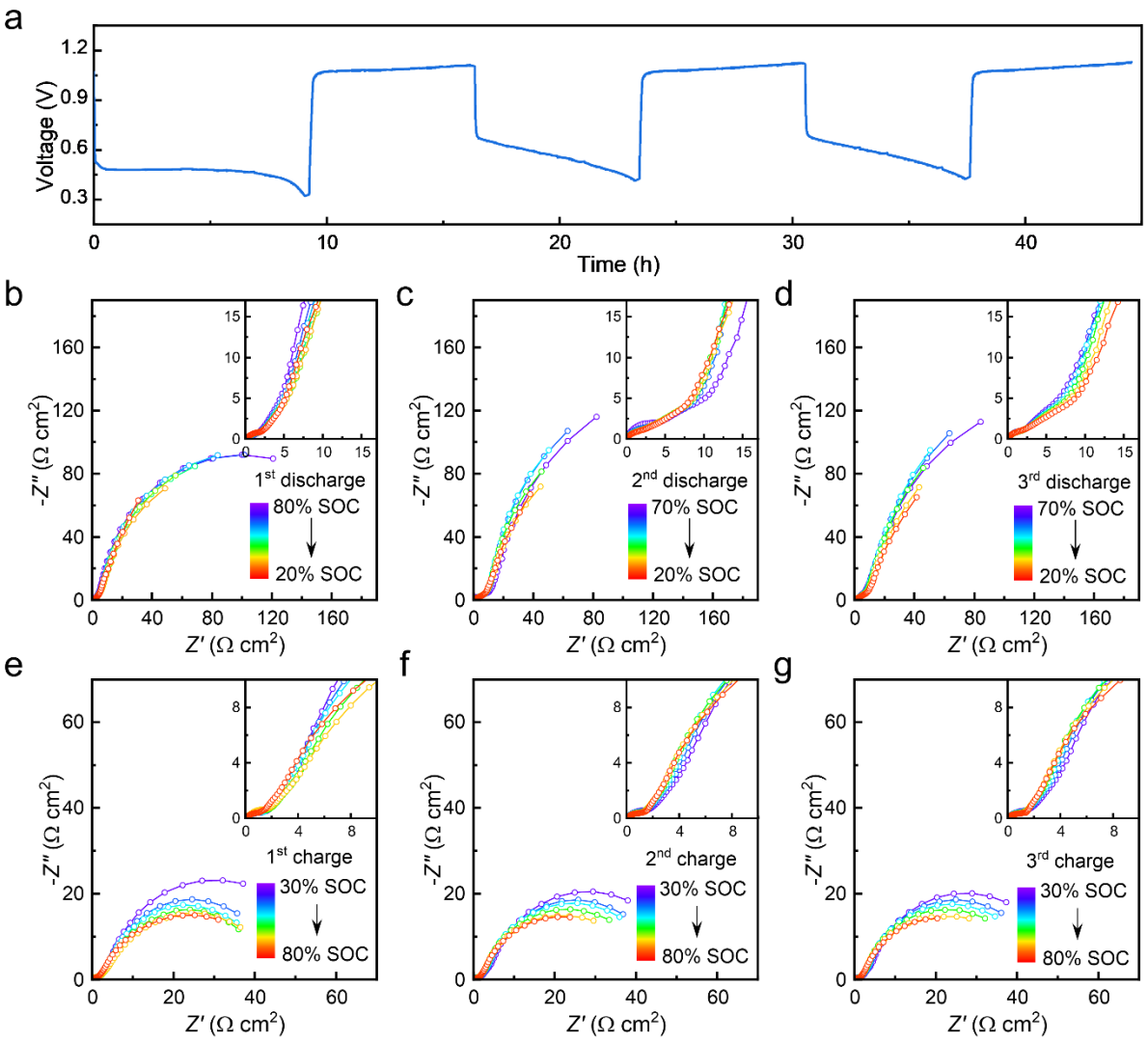


**Supplementary Fig. 29|*In situ* GEIS measurements of sulfur electrode at different state of charge (SOC) with $ZnSO_4$–$ZnI_2$–$H_2O$ electrolyte.** (a) Potential profiles and (b–g) SOC–dependent impedance spectra in the initial three cycling process. The insets are the partially enlarged images of high–frequency region.

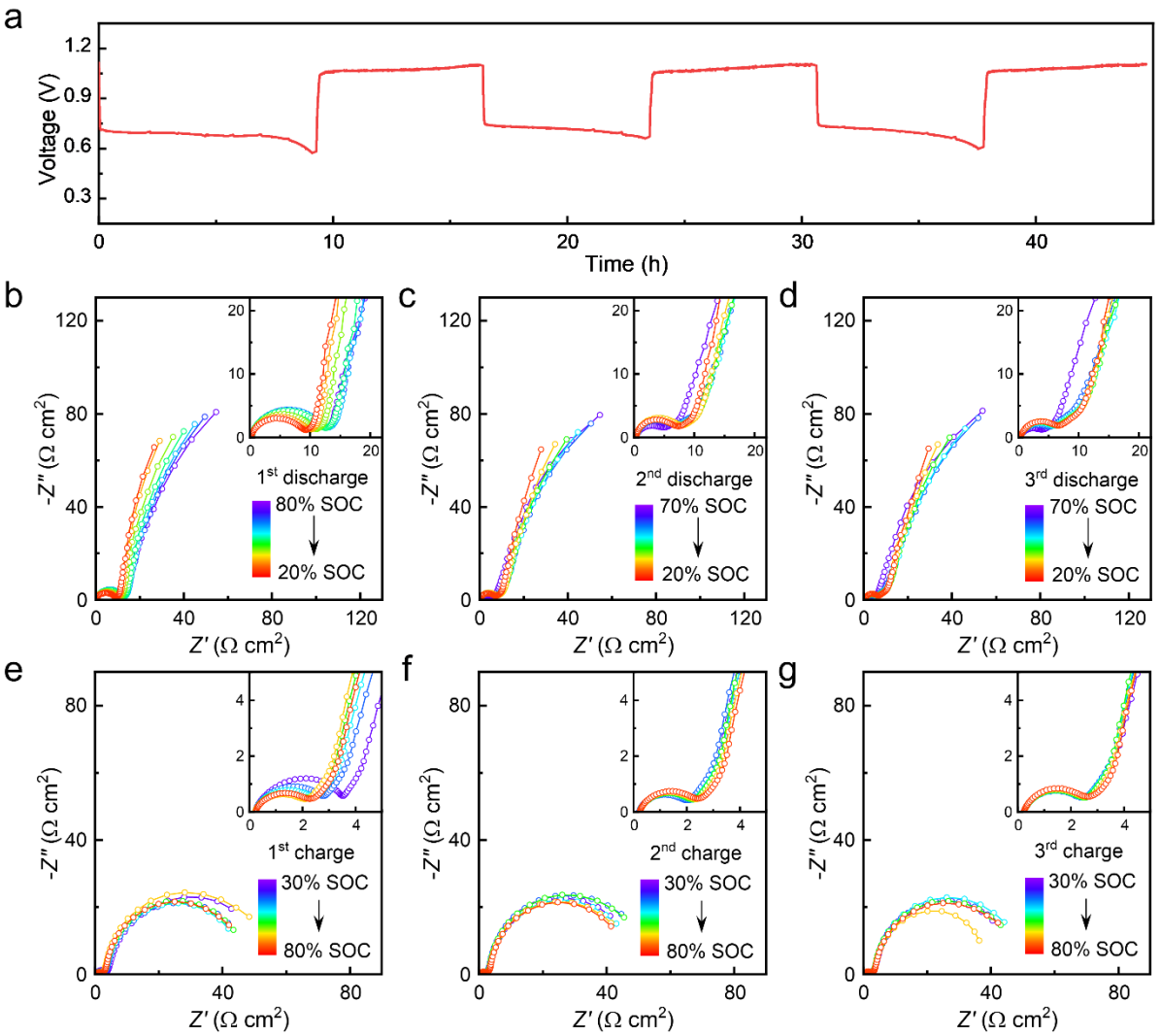


**Supplementary Fig. 30|*In situ* GEIS measurements of sulfur electrode at different state of charge (SOC) with $ZnSO_4$−$ZnI_2$−$H_2O$−DMF electrolyte.** (a) Potential profiles and (b–g) SOC−dependent impedance spectra in the initial three cycling process. The insets are the partially enlarged images of high–frequency region.

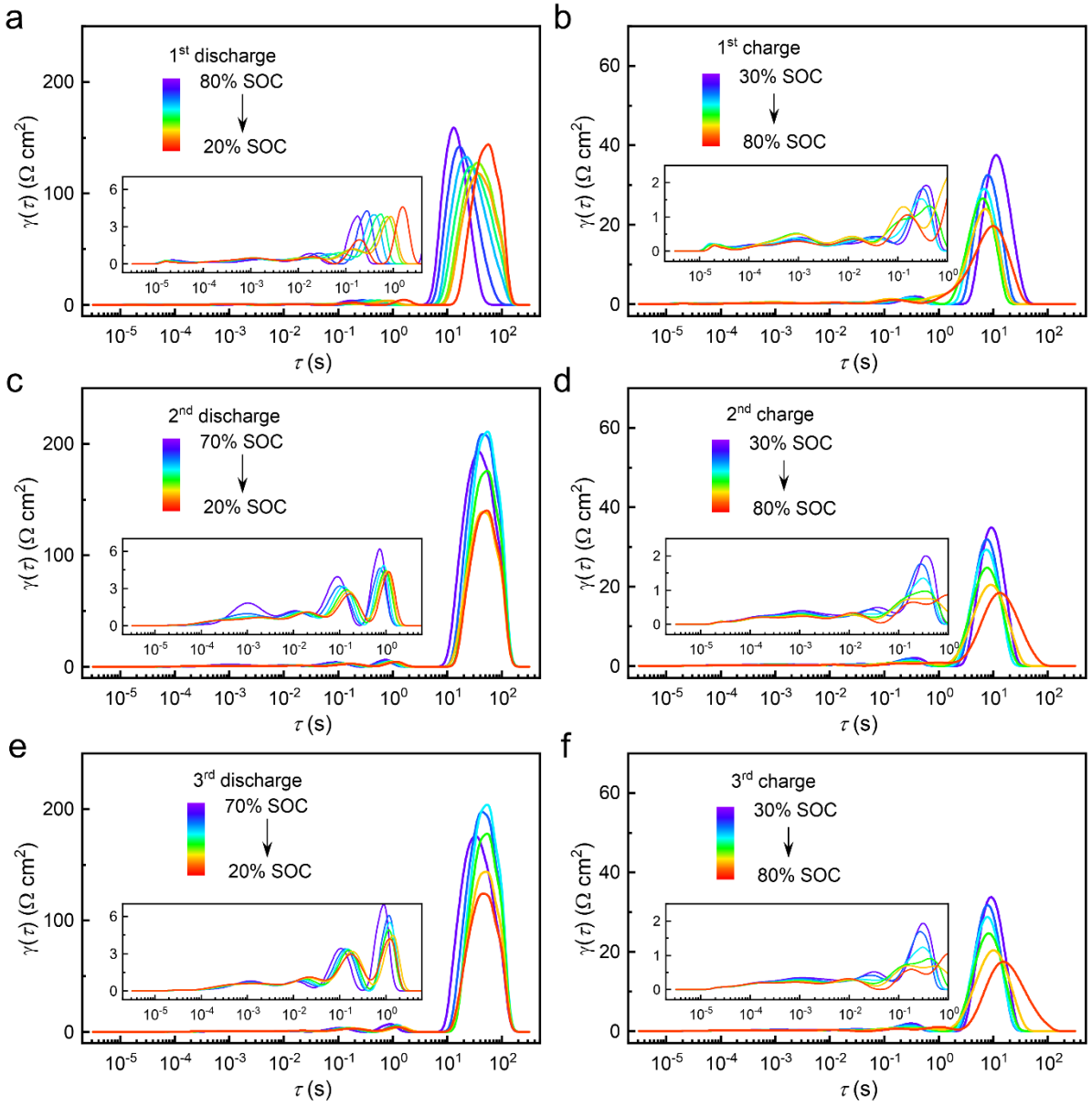


**Supplementary Fig. 31**|DRT analysis of SOC−dependent impedance spectra obtained from *in situ* GEIS measurements of sulfur electrode with $ZnSO_4$−$ZnI_2$−$H_2O$ electrolyte in the (a) 1st−cycle discharging, (b) 1st−cycle charging, (c) 2nd−cycle discharging, (d) 2nd−cycle charging, (e) 3rd−cycle discharging, (f) 3rd−cycle charging processes.

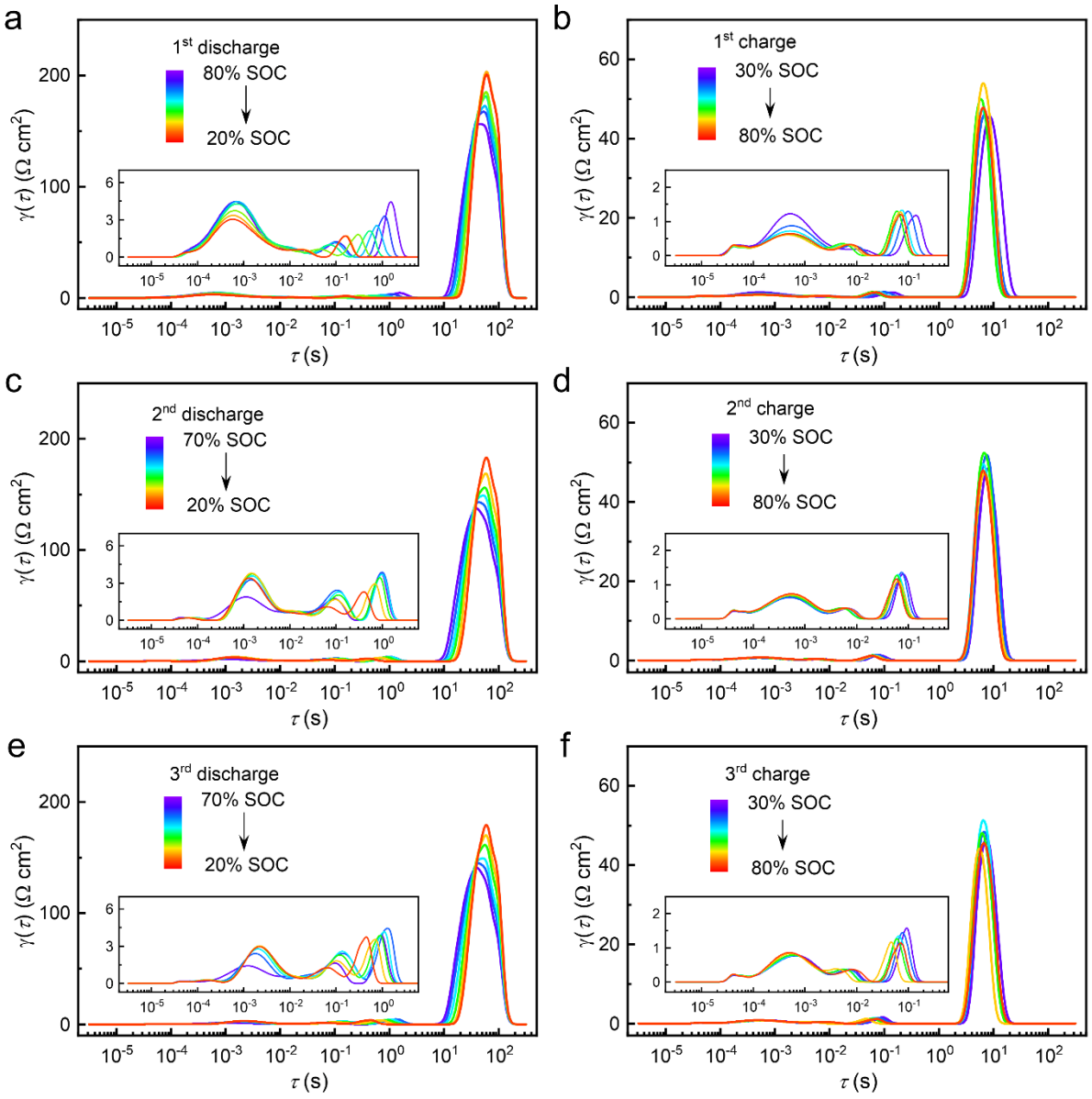


**Supplementary Fig. 32**|DRT analysis of SOC−dependent impedance spectra obtained from *in situ* GEIS measurements of sulfur electrode with $ZnSO_4$−$ZnI_2$−$H_2O$−DMF electrolyte in the (a) 1st−cycle discharging, (b) 1st−cycle charging, (c) 2nd−cycle discharging, (d) 2nd−cycle charging, (e) 3rd−cycle discharging, (f) 3rd−cycle charging processes.

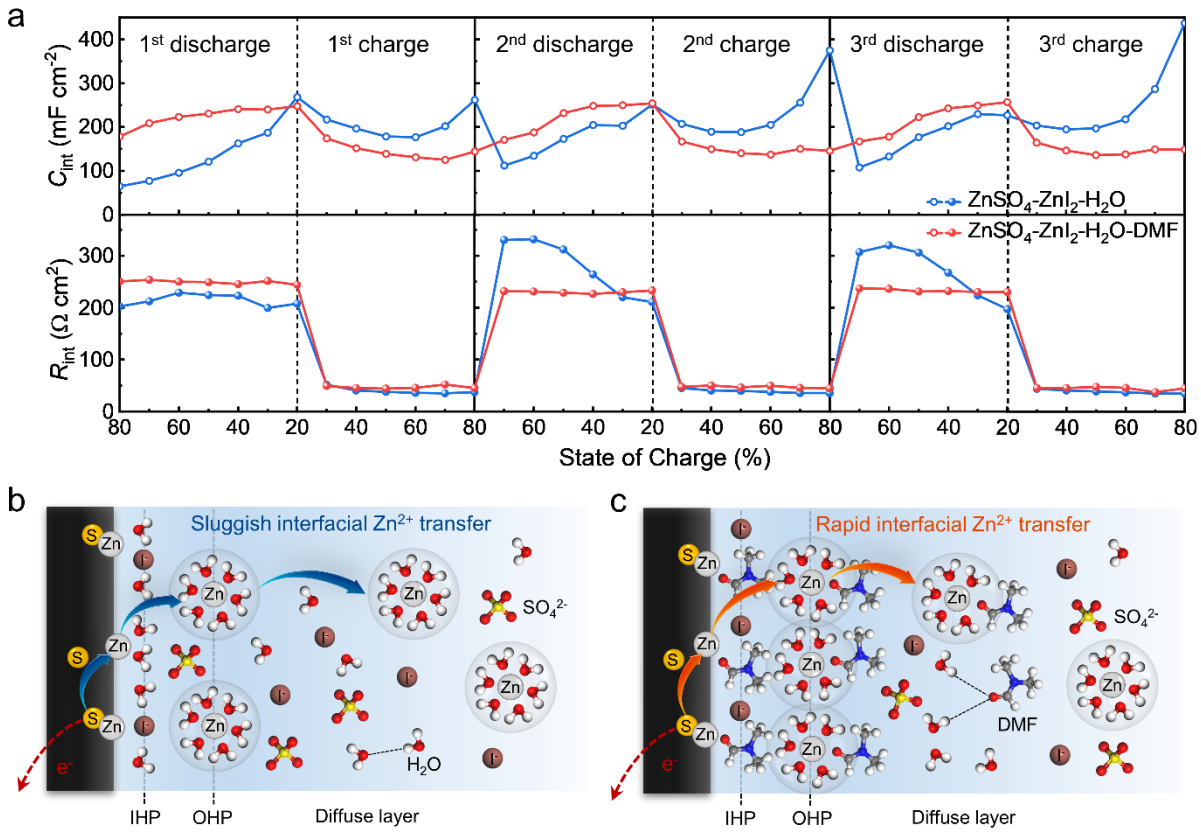


**Supplementary Fig. 33**|(a) The interfacial capacitance and $Zn^{2+}$ transfer resistance variation with the state of charge (SOC). (b, c) Schematic of interfacial EDL structure of sulfur electrodes during charging in different electrolytes.

**Note:** During the initial charging process without the electrochemical oxidation of ZnS, the interfacial capacitance ($C_{int}$) of sulfur electrodes in the $ZnSO_4$–$ZnI_2$–$H_2O$–DMF electrolyte is higher than that in the $ZnSO_4$–$ZnI_2$–$H_2O$ electrolyte (Fig. 3e), indicating that more positively charged zinc ions would be accumulated in the outer Helmholtz plane, which should also be caused by the preferential adsorption of $I^-$ and DMF (Supplementary Fig. 33b,c). However, once the electrochemical oxidation of ZnS occurs, numerous zinc ions would be produced in the sulfur electrodes. Due to the rapid interfacial $Zn^{2+}$ transfer in the $ZnSO_4$–$ZnI_2$–$H_2O$–DMF electrolyte, the $C_{int}$ declines sharply to a level lower than that in the $ZnSO_4$–$ZnI_2$–$H_2O$ electrolyte (Supplementary Fig. 33a). In addition, a rapid increase of $C_{int}$ can be observed when the state of charge is more than 60% in the $ZnSO_4$–$ZnI_2$–$H_2O$ electrolyte. This suggests that the surface charge of sulfur electrodes changes into positive and plentiful $I^-$ ions begin to enter into the outer Helmholtz plane (OHP) region due to the electrostatic interaction.

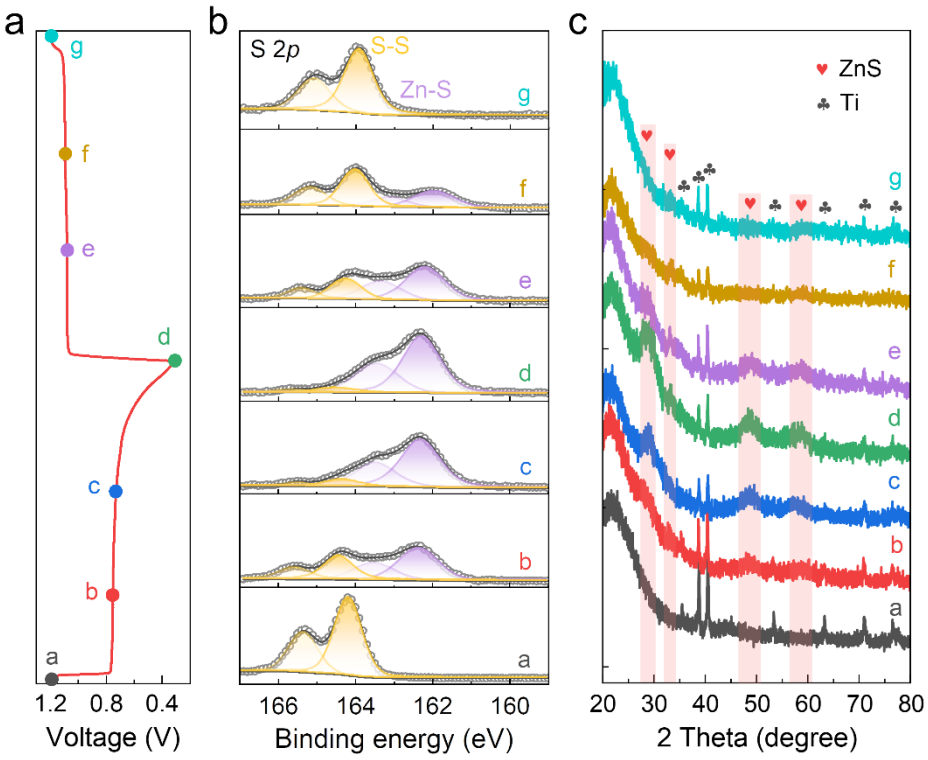


**Supplementary Fig. 34 | *Ex situ* spectroscopic characterization of sulfur electrode in $ZnSO_4$–$ZnI_2$–$H_2O$–DMF electrolyte at different states during the discharging and charging processes.** (a) Potential profile, (b) XPS spectra of S 2*p*, and (c) XRD patterns.

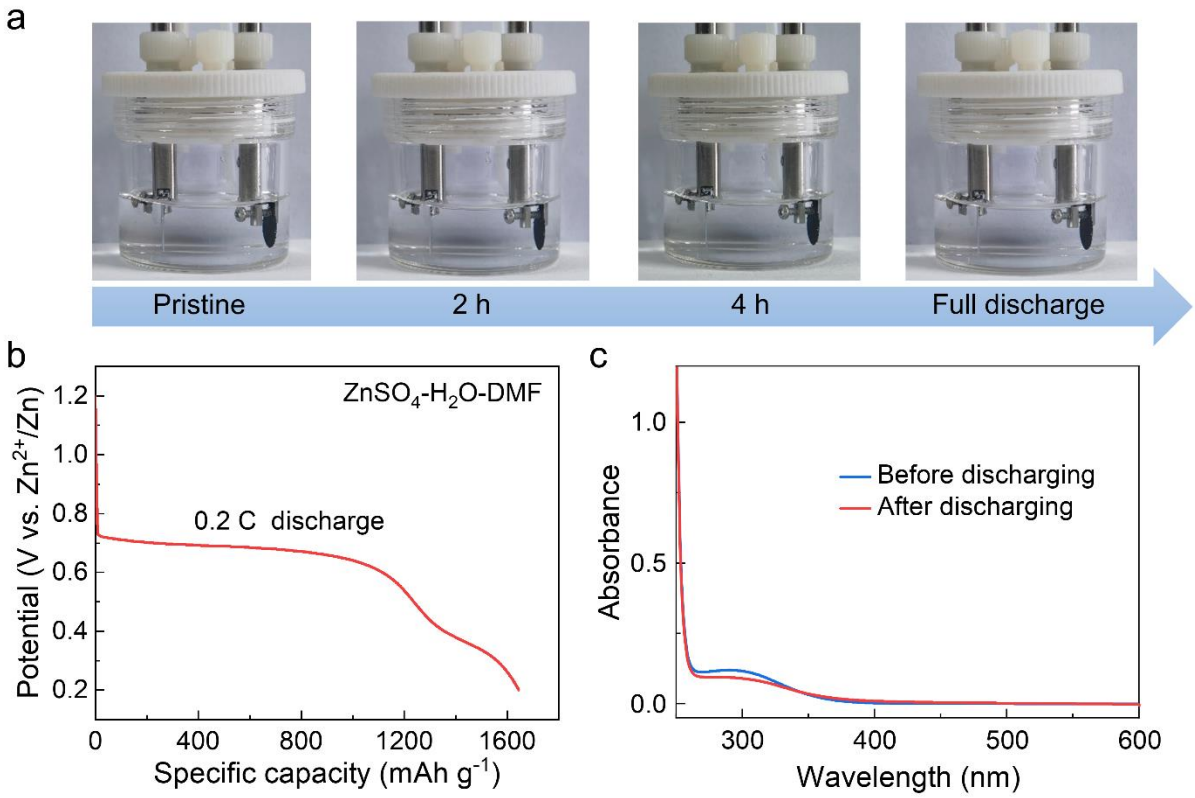


**Supplementary Fig. 35**|(a) The optical electrochemical Zn||S cells for visually observing the discharging process of sulfur electrode. (b) The discharging curve of sulfur electrode in $ZnSO_4$−$ZnI_2$−$H_2O$−DMF electrolyte at 0.2 C. (c) UV-vis spectra of the electrolyte before and after the discharge of sulfur electrode.

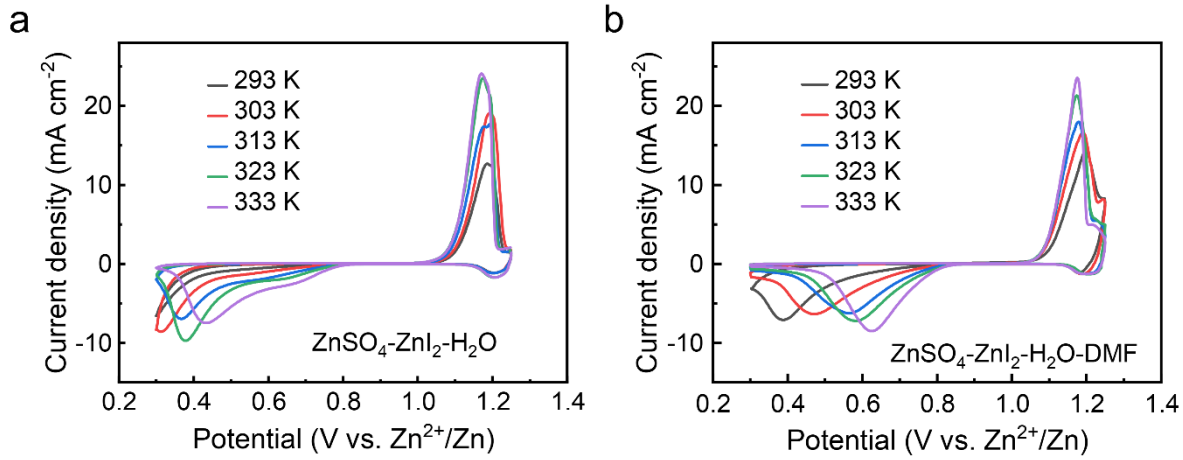


**Supplementary Fig. 36**|CV profiles of sulfur electrodes in the (a) $ZnSO_4$–$ZnI_2$–$H_2O$ and (b) $ZnSO_4$–$ZnI_2$–$H_2O$–DMF electrolytes at different temperatures.

**Note:** The reductive current density $J$ at 0.75 V vs. $Zn^{2+}$/Zn can be obtained from the CV profiles. And the activation energy of sulfur reduction reaction can be calculated according to the Arrhenius equation $J = A*e\hat{}(-E_a/RT)$, where A is a constant, R is the gas constant (8.314 J $mol^{-1}$ $K^{-1}$), T is the thermodynamic temperature (K), and $E_a$ is the apparent activation energy. The result indicates that sulfur electrode in the $ZnSO_4$–$ZnI_2$–$H_2O$–DMF electrolyte show higher reductive current with the lower activation energy of reaction.

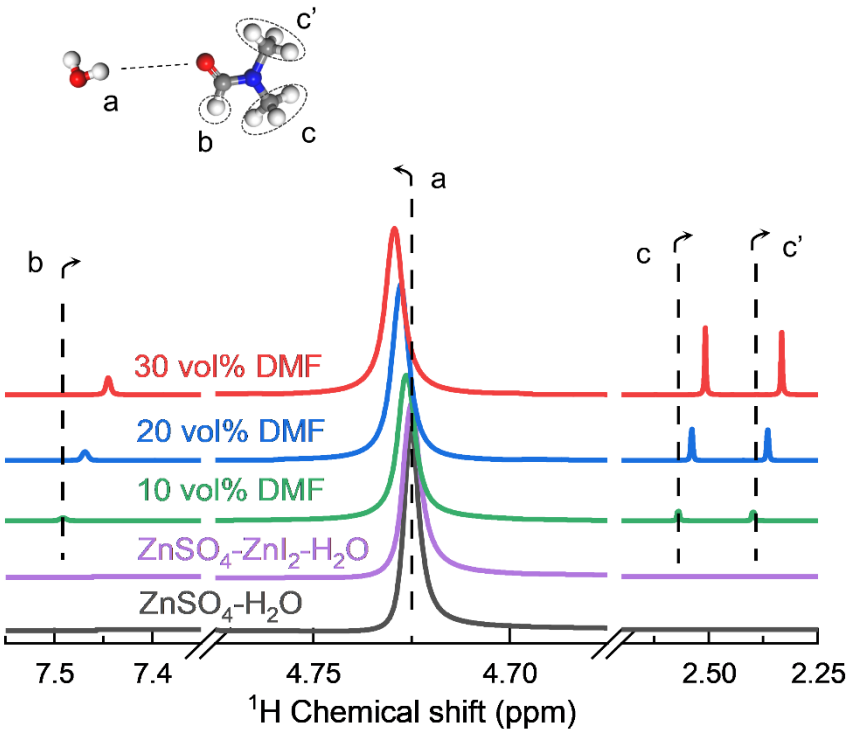


**Supplementary Fig. 37**| $^{1}$H NMR spectra of different electrolytes, including $ZnSO_4$−$H_2O$, $ZnSO_4$−$ZnI_2$−$H_2O$, $ZnSO_4$−$ZnI_2$−$H_2O$−DMF electrolytes with different concentration of DMF.

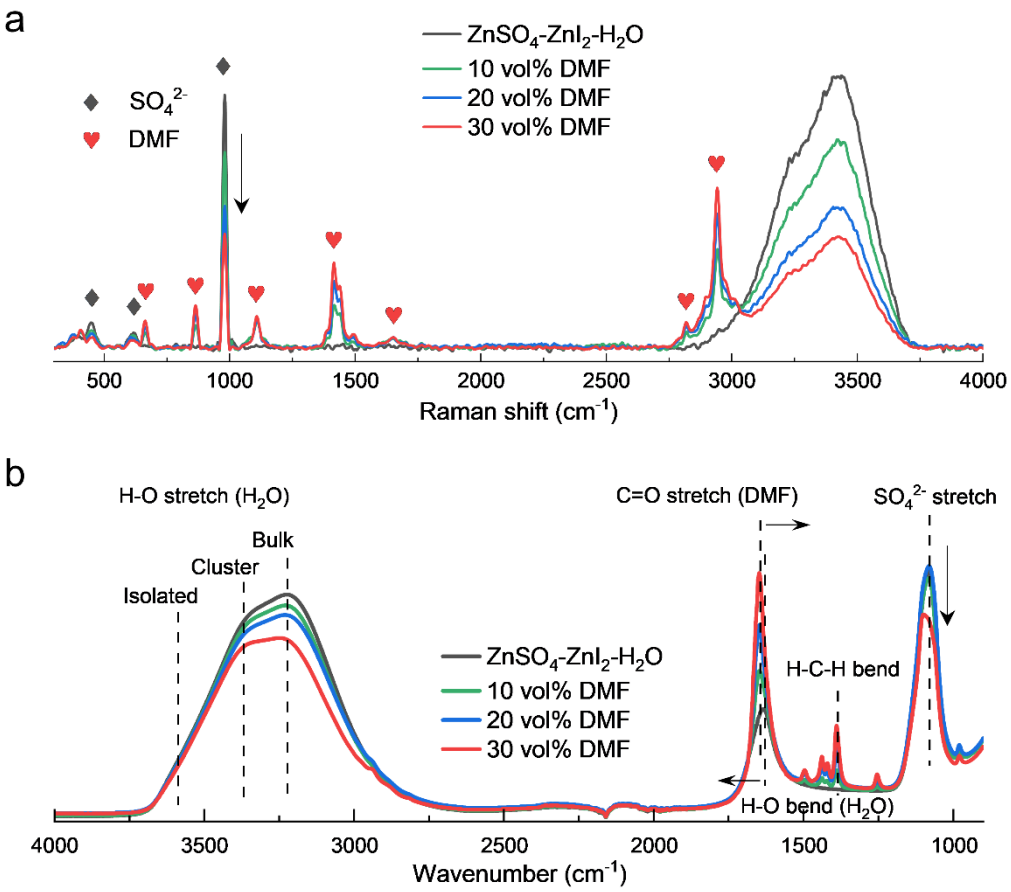


**Supplementary Fig. 38 |** The full (a) Raman and (b) FTIR spectra of $ZnSO_4$–$ZnI_2$–$H_2O$ electrolytes with different concentration of DMF.

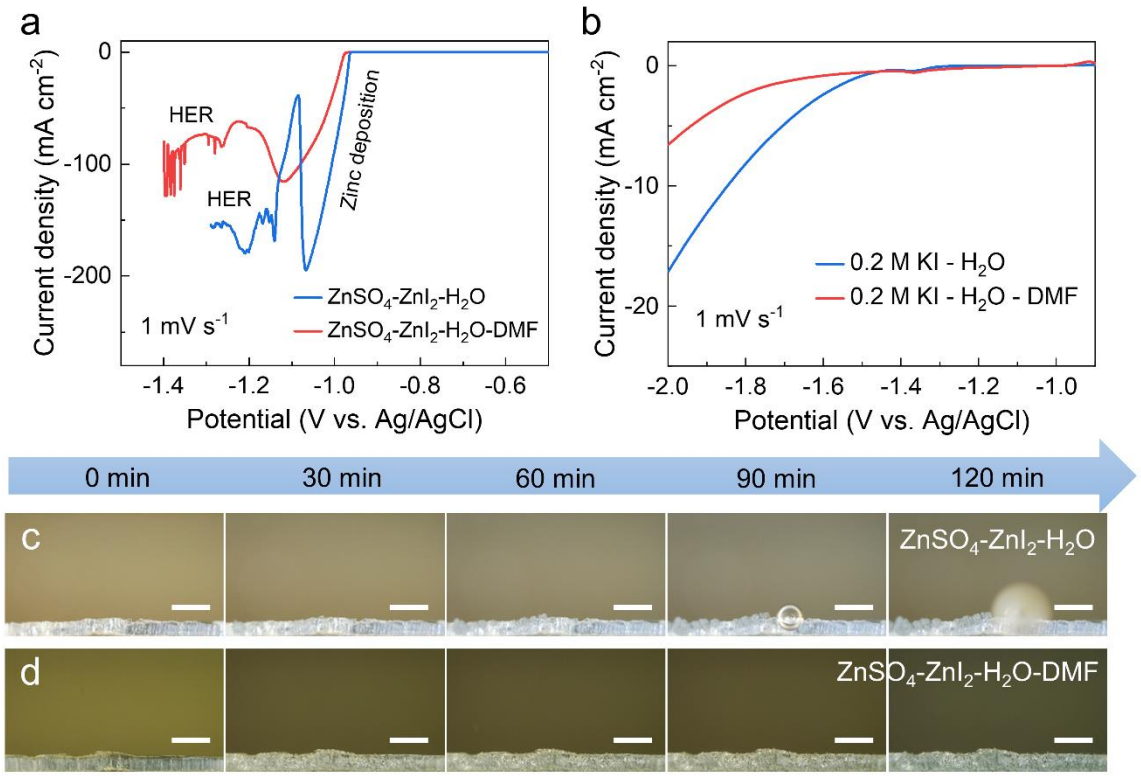


**Supplementary Fig. 39**| (a) LSV curves of Ti mesh in the $ZnSO_4$–$ZnI_2$–$H_2O$ and $ZnSO_4$–$ZnI_2$–$H_2O$–DMF electrolytes at the scan rate of 1 mV $s^{-1}$. Three–electrode Swagelok cells were assembled by utilizing Ti mesh (diameter of 10 mm) as the working electrode, Zn foil (diameter of 12 mm) as the counter electrode, and Ag/AgCl (saturated KCl solution) as the reference electrode, respectively. (b) LSV curves of Zn foil in the 0.2 M KI–$H_2O$ and 0.2 M KI–$H_2O$–DMF electrolytes at the scan rate of 1 mV $s^{-1}$. Three–electrode Swagelok cells were assembled by applying Zn foil (diameter of 12 mm) as the working electrode, carbon paper (diameter of 12 mm) as the counter electrode, and Ag/AgCl (saturated KCl solution) as the reference electrode, respectively. Optical images of Zn foils in (c) $ZnSO_4$–$ZnI_2$–$H_2O$ and (d) $ZnSO_4$–$ZnI_2$–$H_2O$–DMF electrolytes observed in symmetric transparent cells cycled at 1 mA $cm^{-2}$ (the scale bar is 200 μm in each image).

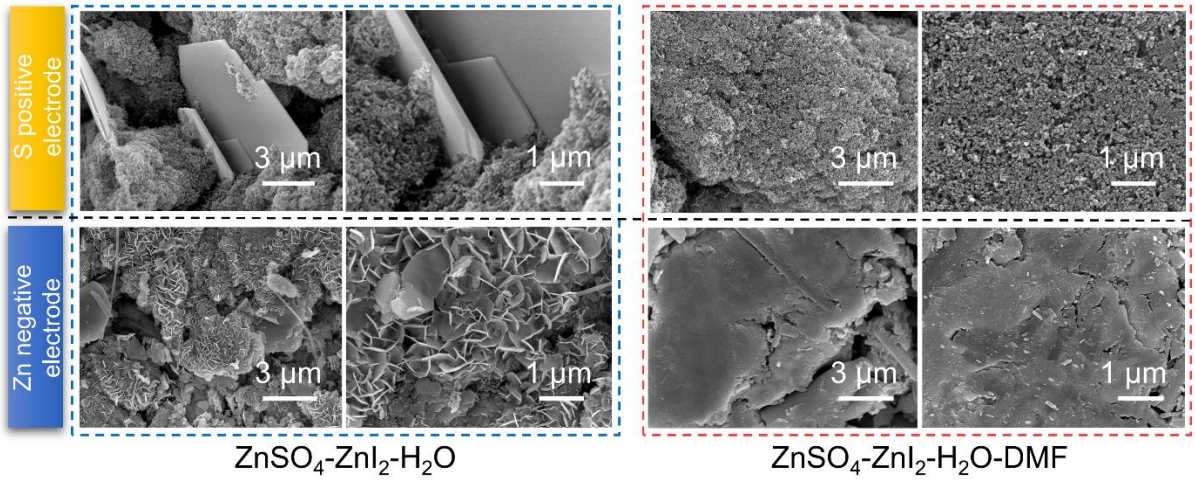


**Supplementary Fig. 40**| SEM images of sulfur positive electrodes and zinc negative electrodes after 150 cycles in the $ZnSO_4$–$ZnI_2$–$H_2O$, and $ZnSO_4$–$ZnI_2$–$H_2O$–DMF electrolytes at 25 ℃ and 1 C.

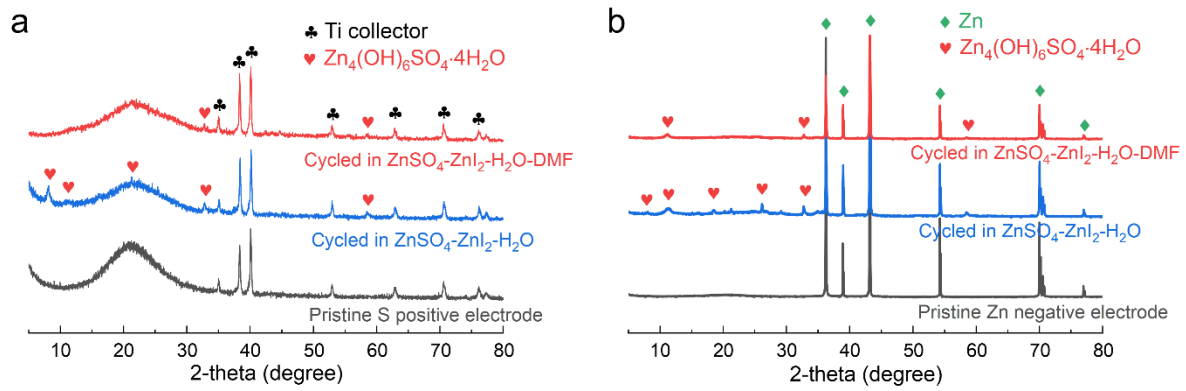


**Supplementary Fig. 41**|XRD patterns of (a) sulfur positive electrodes and (b) zinc negative electrodes after 150 cycles in the $ZnSO_4$–$ZnI_2$–$H_2O$, and $ZnSO_4$–$ZnI_2$–$H_2O$–DMF electrolytes at 25 ℃ and 1 C.

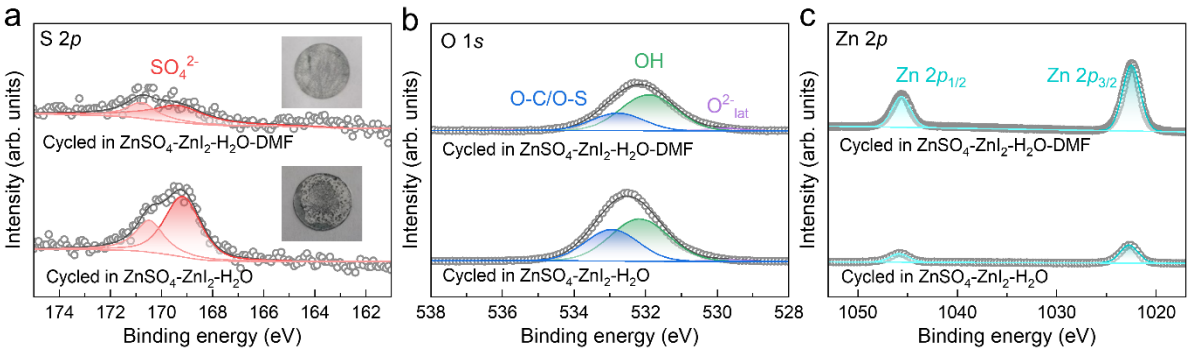


**Supplementary Fig. 42**|XPS profiles of (a) S 2*p*, (b) O 1*s*, and (c) Zn 2*p* peaks for zinc negative electrodes after 100 cycles in $ZnSO_4$–$ZnI_2$–$H_2O$, and $ZnSO_4$–$ZnI_2$–$H_2O$–DMF electrolytes at 25 ℃ and 1 C. The insets are the optical photographs of cycled zinc negative electrodes, which have been washed thoroughly with deionized water and anhydrous ethanol.

**Note:** In the XPS spectra of S 2*p*, only two characteristic peaks can be observed at 169.2 eV and 170.5 eV, which correspond to the $SO_4^{2-}$ species on the surface of zinc negative electrode. Compared with cycled zinc negative electrode in $ZnSO_4$–$ZnI_2$–$H_2O$ electrolyte, the zinc negative electrode after cycled in $ZnSO_4$–$ZnI_2$–$H_2O$–DMF electrolyte shows a significantly weakened $SO_4^{2-}$ signal, implying the suppressed generation of zinc sulfate hydroxide by–products. This also can be confirmed by the XPS spectra of O 1*s*, in which the cycled zinc negative electrode in $ZnSO_4$–$ZnI_2$–$H_2O$–DMF electrolyte could demonstrate the attenuated intensity response in comparison with that in $ZnSO_4$–$ZnI_2$–$H_2O$ electrolyte. Besides, in the XPS spectra of Zn 2*p*, the zinc negative electrode after cycled in $ZnSO_4$–$ZnI_2$–$H_2O$–DMF electrolyte exhibits a stronger intensity response than that in $ZnSO_4$–$ZnI_2$–$H_2O$ electrolyte, which should be resulted from the less by–products formation and more metallic Zn exposed on the surface. Moreover, as presented from the optical photographs of cycled zinc negative electrodes in the inset of Supplementary Fig. 42a, the zinc negative electrode after cycled in $ZnSO_4$–$ZnI_2$–$H_2O$–DMF electrolyte shows much less white products and black spots on the surface, visually demonstrating the inhibited generation of zinc sulfate hydroxide by–products.

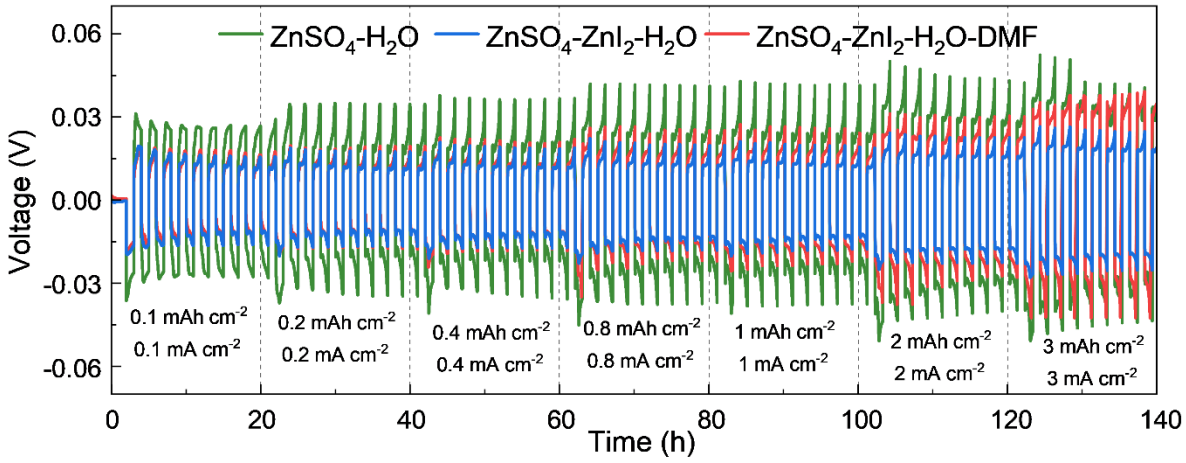


**Supplementary Fig. 43 |** The charge–discharge profiles of Zn||Zn symmetric cells under different current density with $ZnSO_4$−$H_2O$, $ZnSO_4$−$ZnI_2$−$H_2O$, and $ZnSO_4$−$ZnI_2$−$H_2O$−DMF electrolytes.

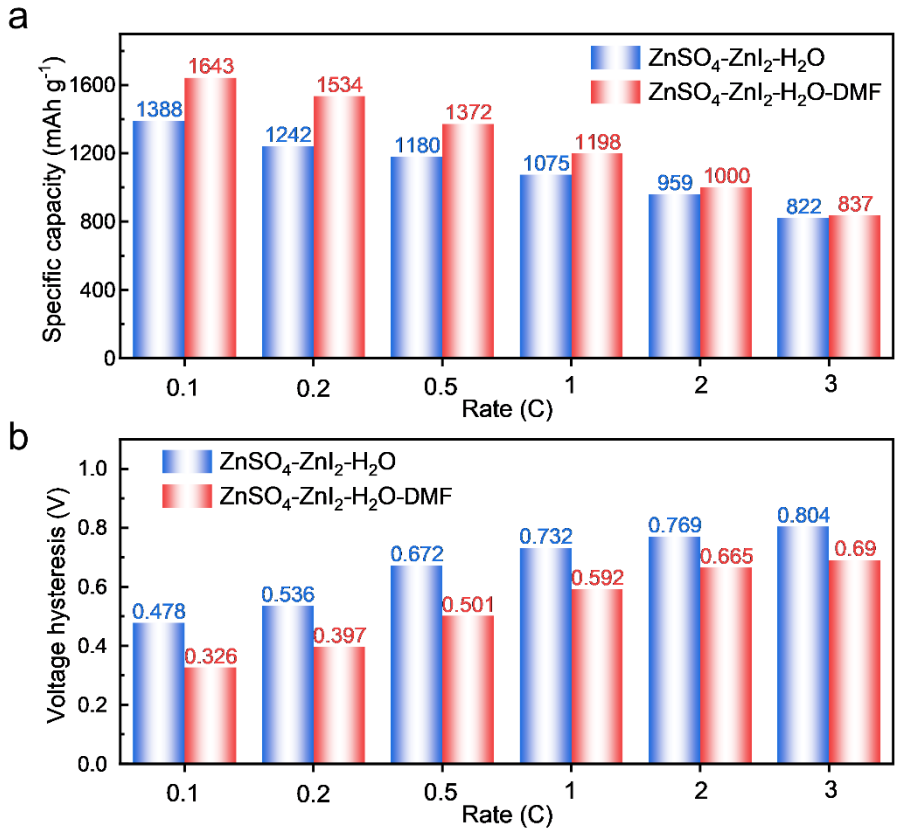


**Supplementary Fig. 44**|(a) Specific capacity and (b) voltage hysteresis of sulfur electrode at different rates in the $ZnSO_4$–$ZnI_2$–$H_2O$, and $ZnSO_4$–$ZnI_2$–$H_2O$–DMF electrolytes.

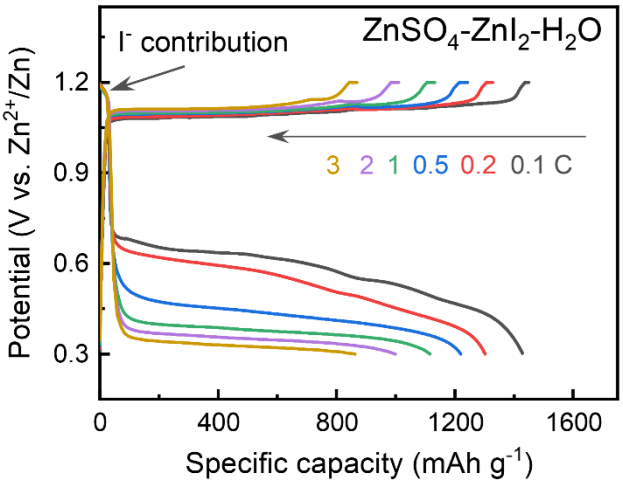


**Supplementary Fig. 45**| Galvanostatic discharge−charge curves of sulfur electrode at different specific current in the $ZnSO_4$−$ZnI_2$−$H_2O$ electrolyte.

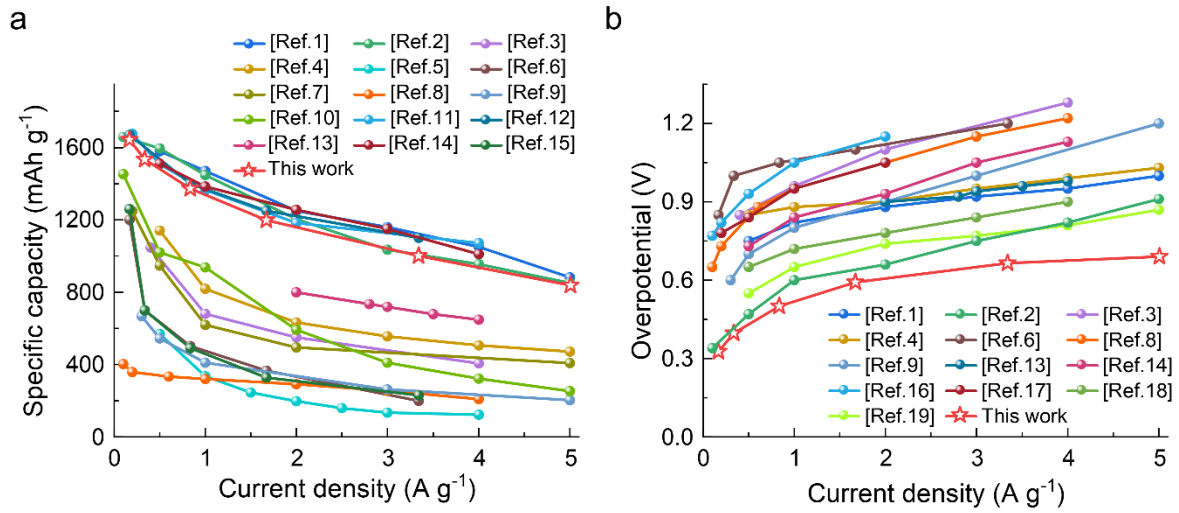


**Supplementary Fig. 46**|Comparisons of (a) specific capacity and (b) overpotential of sulfur electrodes for aqueous Zn||S cells achieved in our work with other reported Zn||S systems[1–19].

**Note:** Our electrolyte system with DMF cosolvent can achieve a specific capacity of 837 mAh $g^{-1}$ at 5 A $g^{-1}$, significantly exceeding the previously reported electrolyte systems with other cosolvents (typically 200–400 mAh $g^{-1}$ at the comparable current density), such as tetraglyme (G4),[4,7,8] ethylene glycol (EG),[6] dimethylacetamide (DMA),[10] and tetramethylene sulfone (TMS)[13]. While the recent Zn||S systems using organoiodide additives,[2,11] Se doping[14] or high–entropy sulfide catalysts[12] could demonstrate the competitively high specific capacity (800–900 mAh $g^{-1}$ at 5 A $g^{-1}$), they often suffer from more severe polarization (typically 0.85–1.2 V) than our system (0.69 V at 5 A $g^{-1}$). The improvement is attributed to the synergistic dual–catalysis of iodide and DMF cosolvent, as well as electric double layer reconstruction, which favor the interfacial $Zn^{2+}$ transfer and enhance reaction kinetics of sulfur conversion.

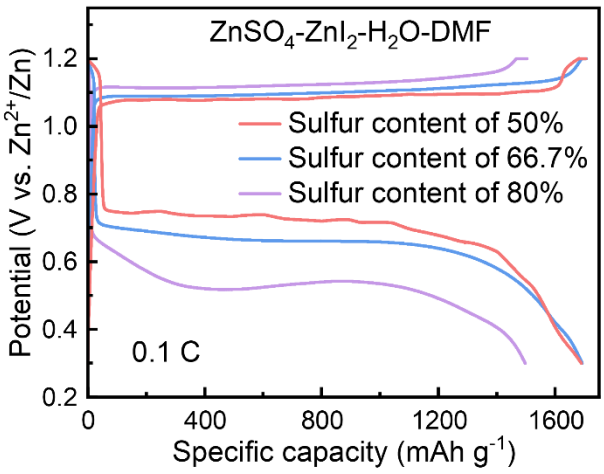


**Supplementary Fig. 47**| Galvanostatic discharge−charge curves of S/KB composites with different sulfur content at 0.1 C (i.e. 0.167 A $g^{-1}$).

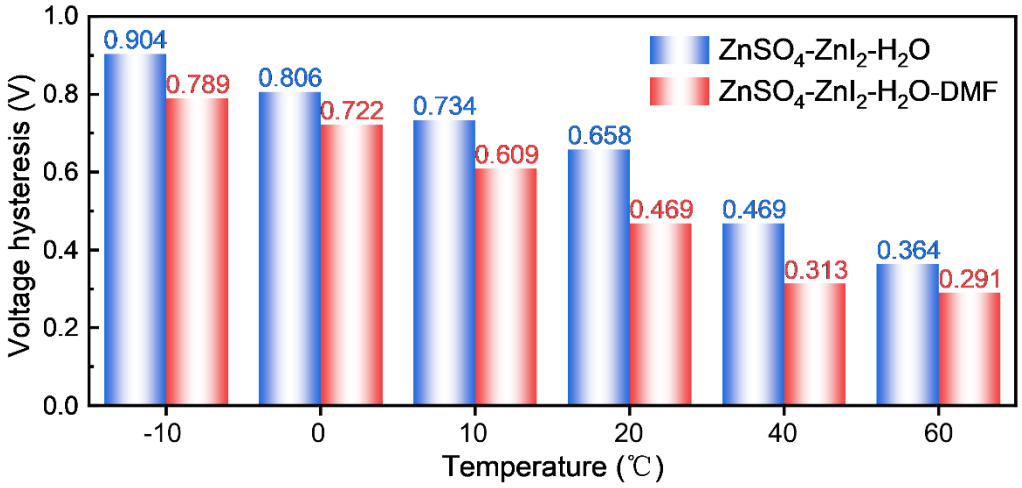


**Supplementary Fig. 48**|Discharge–charge voltage hysteresis of sulfur electrode at different temperatures in the $ZnSO_4$−$ZnI_2$−$H_2O$, and $ZnSO_4$−$ZnI_2$−$H_2O$−DMF electrolytes.

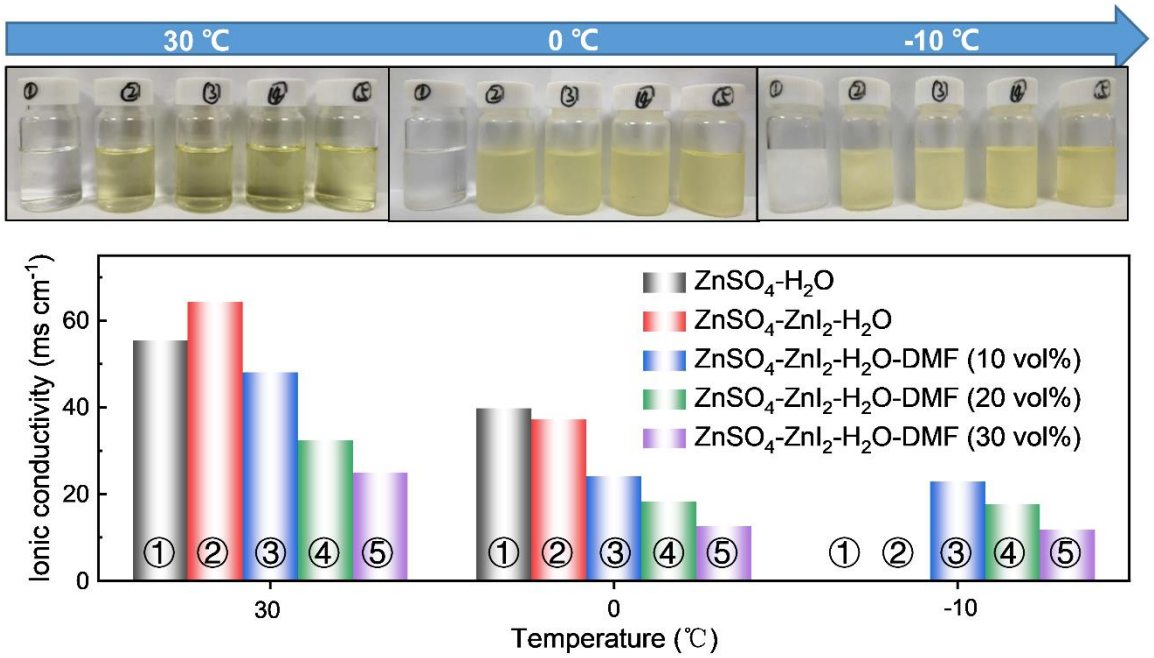


**Supplementary Fig. 49**|Optical pictures and the measured ionic conductivity of different electrolytes at the temperature of 30, 0 and –10 ℃, including the $ZnSO_4$–$H_2O$, $ZnSO_4$–$ZnI_2$–$H_2O$, and $ZnSO_4$–$ZnI_2$–$H_2O$–DMF (10, 20, 30 vol%) electrolytes. At the low temperature of –10 ℃, the $ZnSO_4$–$H_2O$ and $ZnSO_4$–$ZnI_2$–$H_2O$ electrolyte would be frozen, resulting in the absence of apparent ionic conductivity value.

**Supplementary Table 1**|Fitting results of DRT spectra of potential–dependent impedance spectra obtained from *in situ* GEIS measurements of sulfur electrode with $ZnSO_4$−$ZnI_2$−$H_2O$ electrolyte in the initial three cycling process.

| | Potential (vs. $Zn^{2+}$/Zn) | $\tau$ (s) | $R_{int}$ ($\Omega$ $cm^2$) | $C_{int}$ (mF $cm^{-2}$) | | Potential (vs. $Zn^{2+}$/Zn) | $\tau$ (s) | $R_{int}$ ($\Omega$ $cm^2$) | $C_{int}$ (mF $cm^{-2}$) |
|---|---|---|---|---|---|---|---|---|---|
| | 0.9 V | 65.37 | 4477.96 | 14.60 | | 0.4 V | 61.56 | 361.89 | 170.11 |
| | 0.8 V | 65.37 | 4172.32 | 15.67 | | 0.5 V | 63.43 | 398.94 | 159.01 |
| | 0.75 V | 63.43 | 3967.22 | 15.99 | | 0.6 V | 65.37 | 408.03 | 160.20 |
| | 0.7 V | 62.18 | 3600.77 | 17.27 | | 0.7 V | 65.37 | 417.47 | 156.58 |
| | 0.65 V | 58.56 | 3062.13 | 19.12 | | 0.8 V | 65.37 | 410.98 | 159.05 |
| 1st | 0.6 V | 42.52 | 2219.93 | 19.15 | 1st | 0.9 V | 65.37 | 400.37 | 163.26 |
| dis. | 0.55 V | 17.64 | 1025.24 | 17.20 | char. | 1.0 V | 60.34 | 334.79 | 180.23 |
| | 0.5 V | 10.80 | 553.61 | 19.52 | | 1.05 V | 17.46 | 94.9 | 184.00 |
| | 0.45 V | 4.90 | 231.18 | 21.21 | | 1.1 V | 5.00 | 31.62 | 158.22 |
| | 0.4 V | 20.70 | 188.96 | 109.53 | | 1.15 V | 60.34 | 48.77 | 1237.24 |
| | 0.35 V | 40.45 | 206.67 | 195.71 | | 1.2 V | 58.56 | 11.26 | 5200.44 |
| | 0.3 V | 46.06 | 207.96 | 221.50 | | | | | |
| | 1.1 V | 58.56 | 458.02 | 127.85 | | 0.4 V | 60.34 | 336.57 | 179.28 |
| | 1.0 V | 64.07 | 1023.21 | 62.62 | | 0.5 V | 62.18 | 372.76 | 166.80 |
| | 0.9 V | 65.37 | 1056.23 | 61.89 | | 0.6 V | 62.18 | 386.38 | 160.92 |
| | 0.8 V | 60.34 | 910.35 | 66.28 | | 0.7 V | 63.43 | 390.94 | 162.26 |
| | 0.75 V | 55.70 | 756.68 | 73.61 | | 0.8 V | 63.43 | 387.64 | 163.64 |
| | 0.7 V | 38.09 | 557.88 | 68.28 | | 0.9 V | 62.18 | 376.32 | 165.23 |
| 2nd | 0.65 V | 20.91 | 348.23 | 60.03 | 2nd | 1.0 V | 60.34 | 333.69 | 180.83 |
| dis. | 0.6 V | 21.54 | 329.13 | 65.45 | char. | 1.05 V | 23.10 | 123.59 | 186.94 |
| | 0.55 V | 24.78 | 338.93 | 73.11 | | 1.1 V | 4.85 | 30.5 | 159.18 |
| | 0.5 V | 32.46 | 253.73 | 127.93 | | 1.15 V | 60.34 | 49.73 | 1213.36 |
| | 0.45 V | 32.46 | 209.13 | 155.21 | | 1.2 V | 60.34 | 10.96 | 5505.50 |
| | 0.4 V | 39.25 | 210.25 | 186.69 | | | | | |
| | 0.35 V | 54.05 | 229.73 | 235.30 | | | | | |
| | 0.3 V | 55.70 | 229.99 | 242.19 | | | | | |
| | 1.1 V | 58.56 | 465.22 | 125.87 | | 0.4 V | 4.13 | 338.32 | 183.78 |
| | 1.0 V | 64.07 | 962.96 | 66.54 | | 0.5 V | 4.16 | 372.51 | 172.00 |
| | 0.9 V | 65.37 | 991.39 | 65.93 | | 0.6 V | 4.16 | 387.44 | 165.37 |
| | 0.8 V | 55.70 | 709.16 | 78.55 | | 0.7 V | 4.16 | 389.64 | 164.44 |
| | 0.75 V | 33.12 | 494.17 | 67.01 | | 0.8 V | 4.18 | 388.37 | 168.31 |
| | 0.7 V | 19.30 | 312.29 | 61.80 | | 0.9 V | 4.18 | 381.64 | 171.28 |
| 3rd | 0.65 V | 22.20 | 318.17 | 69.77 | 3rd | 1.0 V | 4.13 | 336.85 | 184.59 |
| dis. | 0.6 V | 35.16 | 387.01 | 90.86 | char. | 1.05 V | 3.37 | 137.46 | 211.54 |
| | 0.55 V | 35.16 | 351.29 | 100.10 | | 1.1 V | 1.58 | 30.59 | 158.71 |
| | 0.5 V | 36.23 | 276.09 | 131.24 | | 1.15 V | 4.1 | 49.19 | 1226.68 |
| | 0.45 V | 35.16 | 219.89 | 159.91 | | 1.2 V | 4.1 | 10.52 | 5735.77 |
| | 0.4 V | 42.52 | 220.68 | 192.68 | | | | | |
| | 0.35 V | 57.40 | 243.07 | 236.14 | | | | | |
| | 0.3 V | 57.40 | 234.78 | 244.47 | | | | | |

**Supplementary Table 2**|Fitting results of DRT spectra of potential–dependent impedance spectra obtained from *in situ* GEIS measurements of sulfur electrode with $ZnSO_4$−$ZnI_2$−$H_2O$−DMF electrolyte in the initial three cycling process.

| | Potential (vs. $Zn^{2+}$/Zn) | $\tau$ (s) | $R_{int}$ ($\Omega$ cm$^2$) | $C_{int}$ (mF cm$^{-2}$) | | Potential (vs. $Zn^{2+}$/Zn) | $\tau$ (s) | $R_{int}$ ($\Omega$ cm$^2$) | $C_{int}$ (mF cm$^{-2}$) |
|---|---|---|---|---|---|---|---|---|---|
| | 1.0 V | 62.80 | 677.58 | 92.69 | | 0.4 V | 60.95 | 307.90 | 197.94 |
| | 0.9 V | 62.18 | 624.03 | 99.64 | | 0.5 V | 62.80 | 336.49 | 186.64 |
| | 0.8 V | 41.26 | 380.39 | 108.48 | | 0.6 V | 64.07 | 343.84 | 186.34 |
| | 0.75 V | 38.09 | 299.48 | 127.19 | | 0.7 V | 64.07 | 342.99 | 186.80 |
| | 0.7 V | 57.40 | 280.28 | 204.79 | | 0.8 V | 64.07 | 343.14 | 186.72 |
| | 0.65 V | 60.34 | 298.87 | 201.90 | | 0.9 V | 64.07 | 346.82 | 184.74 |
| 1st | 0.6 V | 60.34 | 295.54 | 204.17 | 1st | 1.0 V | 64.07 | 351.42 | 182.32 |
| dis. | 0.55 V | 60.34 | 280.17 | 215.37 | char. | 1.05 V | 18.36 | 103.98 | 176.54 |
| | 0.5 V | 60.34 | 274.99 | 219.43 | | 1.1 V | 5.93 | 44.40 | 133.56 |
| | 0.45 V | 59.15 | 261.56 | 226.13 | | 1.15 V | 62.80 | 45.98 | 1365.87 |
| | 0.4 V | 59.15 | 252.86 | 233.91 | | 1.2 V | 43.38 | 8.90 | 4874.17 |
| | 0.35 V | 59.15 | 245.68 | 240.74 | | | | | |
| | 0.3 V | 59.15 | 246.34 | 240.10 | | | | | |
| | 1.1 V | 64.72 | 531.72 | 121.71 | | 0.4 V | 60.95 | 308.66 | 197.46 |
| | 1.0 V | 64.72 | 712.97 | 90.77 | | 0.5 V | 60.95 | 335.11 | 181.87 |
| | 0.9 V | 64.72 | 654.42 | 98.89 | | 0.6 V | 62.80 | 341.38 | 183.97 |
| | 0.8 V | 20.09 | 216.10 | 92.95 | | 0.7 V | 62.80 | 339.10 | 185.20 |
| | 0.75 V | 22.65 | 206.95 | 109.43 | | 0.8 V | 59.15 | 276.69 | 213.76 |
| | 0.7 V | 57.40 | 276.92 | 207.27 | | 0.9 V | 62.80 | 341.43 | 183.94 |
| 2nd | 0.65 V | 59.15 | 277.59 | 213.07 | 2nd | 1.0 V | 62.80 | 350.59 | 179.14 |
| dis. | 0.6 V | 59.15 | 273.82 | 216.00 | char. | 1.05 V | 22.65 | 135.08 | 167.65 |
| | 0.55 V | 59.15 | 276.69 | 213.76 | | 1.1 V | 5.16 | 42.97 | 119.97 |
| | 0.5 V | 59.15 | 279.30 | 211.76 | | 1.15 V | 62.80 | 44.95 | 1397.17 |
| | 0.45 V | 59.15 | 263.72 | 224.27 | | 1.2 V | 57.40 | 9.73 | 5899.02 |
| | 0.4 V | 59.15 | 257.86 | 229.37 | | | | | |
| | 0.35 V | 59.15 | 254.41 | 232.48 | | | | | |
| | 0.3 V | 59.15 | 255.40 | 231.58 | | | | | |
| | 1.1 V | 64.72 | 514.79 | 125.71 | | 0.4 V | 62.80 | 314.32 | 199.81 |
| | 1.0 V | 64.72 | 715.64 | 90.43 | | 0.5 V | 62.80 | 341.34 | 183.99 |
| | 0.9 V | 64.72 | 655.51 | 98.73 | | 0.6 V | 62.80 | 345.06 | 182.01 |
| | 0.8 V | 13.87 | 142.19 | 97.57 | | 0.7 V | 64.72 | 342.33 | 189.04 |
| | 0.75 V | 42.10 | 236.20 | 178.23 | | 0.8 V | 64.72 | 342.91 | 188.72 |
| | 0.7 V | 59.15 | 283.30 | 208.77 | | 0.9 V | 64.72 | 349.72 | 185.05 |
| 3rd | 0.65 V | 60.95 | 296.10 | 205.83 | 3rd | 1.0 V | 62.80 | 356.16 | 176.33 |
| dis. | 0.6 V | 60.95 | 286.30 | 212.88 | char. | 1.05 V | 5.75 | 43.62 | 189.15 |
| | 0.55 V | 60.95 | 286.82 | 212.49 | | 1.1 V | 32.79 | 173.33 | 131.93 |
| | 0.5 V | 60.95 | 280.62 | 217.19 | | 1.15 V | 62.80 | 43.81 | 1433.53 |
| | 0.45 V | 59.15 | 274.75 | 215.27 | | 1.2 V | 57.40 | 9.44 | 6080.24 |
| | 0.4 V | 59.15 | 272.79 | 216.82 | | | | | |
| | 0.35 V | 59.15 | 266.09 | 222.28 | | | | | |
| | 0.3 V | 59.15 | 251.84 | 234.85 | | | | | |

**Supplementary Table 3**|Comparison of the cycle performance of Zn||S battery achieved in this work with recently reported state−of−art aqueous Zn||S batteries.

| Electrolyte | Positive electrode | S loading (mg $cm^{-2}$) | Capacity (mAh $g^{-1}$) | Decay rate per cycle (%) | Ref. |
|---|---|---|---|---|---|
| 2 M $ZnSO_4$ + 0.2 M $ZnI_2$ + DMF:$H_2O$ (3:7 vol.) | 53.8 % S/KB* | 1.5−2.0 | 610 ($1000^{th}$ cycle, 2 C)# | 0.034 | This work |
| 3 M $ZnSO_4$ + 0.05M $ZnI_2$ | 55 % S/KB* | 1.4−1.6 | 882 ($550^{th}$ cycle, 5 A $g^{-1}$) | — | 1 |
| 3 M $ZnSO_4$ + 0.075 M $ZnI_2$ | 41 % S/S,N–codoped carbon nanofibers | 1.0−2.0 | 699 ($300^{th}$ cycle, 4 A $g^{-1}$) | 0.18 | 20 |
| 1 M $Zn(OAc)_2$ + 0.25 M $Me_3PhN^+I^-$ | 54 % S/KB* | 3.0 | 314 ($500^{th}$ cycle, 3 A $g^{-1}$) | 0.11 | 2 |
| 2 M $Zn(OTF)_2$+ 0.15 wt% $I_2$ + G4:$H_2O$ (2:3 vol.)* | 53.7 % S/HCS* | 1.2−1.6 | 347 ($600^{th}$ cycle, 4 A $g^{-1}$) | 0.05 | 4 |
| 2 M $Zn(OTF)_2$ + 0.15wt% $I_2$ + G4:$H_2O$ (2:3 vol.)* | SPAN* | 1.2 | 466 ($800^{th}$ cycle, 2 A $g^{-1}$) | 0.023 | 7 |
| 1 M $Zn(OTF)_2$ +0.05 M $ZnI_2$ + PM:$H_2O$ (3:2 vol.)* | 70 % S/porous carbon | 1.5 | 480 ($1200^{th}$ cycle, 3 A $g^{-1}$) | 0.025 | 21 |
| 2 M $Zn(OTF)_2$ + 0.05 M $ZnI_2$ + EG:$H_2O$ (1:1 vol.)* | 50 % S/nanoporous carbon | 3.0 | 350 ($250^{th}$ cycle, 3 A $g^{-1}$) | 0.12 | 22 |
| 1 M $Zn(OAc)_2$ + 0.05 wt% $I_2$ + EG:$H_2O$ (1:9 vol.)* | 48 % S/Vulcan carbon | — | 316 ($600^{th}$ cycle, 1 C) | 0.032 | 6 |
| $Zn(CH_3COO)_2$ + $I_2$ + EG:$H_2O$ (2:1 wt.)* | 60 % S/porous carbon nanofibers | — | 225 ($500^{th}$ cycle, 1 A $g^{-1}$) | 0.11 | 23 |
| 2 M $ZnSO_4$ + 2 mg $mL^{-1}$ TU* | 33.3 % S/KB* | 1.0 | 764 ($300^{th}$ cycle, 5 A $g^{-1}$) | 0.11 | 19 |
| 2 M $ZnSO_4$ + 0.05 M $ZnI_2$ + 0.05 M TU* | ZnS | 2.5 | 433 ($300^{th}$ cycle, 2 A $g^{-1}$) | 0.156 | 24 |

**Supplementary Table 3** (continued)

| Electrolyte | Positive electrode | S loading (mg $cm^{-2}$) | Capacity (mAh $g^{-1}$) | Decay rate per cycle (%) | Ref. |
|---|---|---|---|---|---|
| 2 M $ZnSO_4$ + 0.2 M $ZnI_2$ + DMF:$H_2O$ (3:7 vol.) | 53.8 % S/KB* | 1.5−2.0 | 610 ($1000^{th}$ cycle, 2 C) | 0.034 | This work |
| $ZnSO_4$-PVA gel electrolyte* | 75 % S/FeNC/NC | 2.0−2.6 | 519 ($300^{th}$ cycle,0.5 A $g^{-1}$) | 0.141 | 25 |
| 1 M $Zn(OTF)_2$ + 0.2 M ChI* | 74.8 % S/Mesoporous carbon | 1.1−1.2 | 980 ($30^{th}$ cycle, 1 A $g^{-1}$) | — | 11 |
| $ZnSO_4$ | S : KB : HES* = 1 : 1 : 0.1 | 2.0−3.0 | 577 ($400^{th}$ cycle, 4 C) | 0.06 | 12 |
| 1M $Zn(OTF)_2$ + 0.05 wt% $I_2$ + DMC:$H_2O$ (4:6 vol.)* | 70 % S/AJPS* | 1.0−2.0 | 180 ($200^{th}$ cycle, 1 A $g^{-1}$) | 0.262 | 16 |
| 1 M $Zn(OTF)_2$ + 1 M LiTFSI + 1 mg $I_2$ + TMS:$H_2O$ (1:2 vol.)* | 49 % S/AC-3000 | 1.0 | 550 ($200^{th}$ cycle,2.8 A $g^{-1}$) | 0.072 | 13 |
| 2 M $Zn(OTF)_2$+ 0.15 wt% $I_2$ + G4:$H_2O$ (2:3 vol.)* | 50 % $Se_{0.06}S_{0.94}$/HCS* | 1.2−1.4 | 735 ($500^{th}$ cycle, 4 A $g^{-1}$) | 0.058 | 14 |
| $ZnSO_4$-PVA gel electrolyte* | 70 % S/Fe-PANi* | 1.8 | — | 0.23 | 17 |
| $ZnSO_4$-PVA gel electrolyte* | 54 % S/NC-CoO | 2.0 | 640 ($500^{th}$ cycle,0.5 A $g^{-1}$) | 0.057 | 26 |
| 2 M $Zn(OTF)_2$ + $ZnI_2$ + $H_2O$:EG (1:1 vol.)* | 52 % S/Fe-NC | 1.0 | 822 ($300^{th}$ cycle, 5 A $g^{-1}$) | 0.147 | 18 |
| $ZnSO_4$ + 0.05 wt% $I_2$ + 5 mM SA* | 50 % S/$Ni_xFe_yO_4$ | — | 280 ($1000^{th}$ cycle, 1 C) | 0.019 | 15 |

* KB = Ketjen black, G4 = tetraglyme, HCS = Hollow carbon sphere, SPAN = Sulfurized polyacrylonitrile, PM = Propylene glycol methyl ether, EG = Ethylene glycol, TU = Thiourea, PVA = polyvinyl alcohol, ChI = Choline iodide, HES = high-entropy sulfide, DMC = dimethyl carbonate, AJPS = Activated jackfruit peel-derived porous carbon, TMS = tetramethylene sulfone, Fe-PANi = $Fe(CN)_6^{4-}$-doped polyaniline, SA = Sulfanilamide. # 1 C = 1.67 A $g^{-1}$, 2 C = 3.34 A $g^{-1}$.

**Note:** the percentages in the column of 'Positive electrode' indicate the sulfur content in the sulfur composites.

## Supplementary References


1. Hei, P. *et al.* Facilitating the Electrochemical Oxidation of ZnS through Iodide Catalysis for Aqueous Zinc–Sulfur Batteries. *Angew. Chem. Int. Ed.* **63**, e202316082 (2024).
2. Wu, W., Wang, S., Lin, L., Shi, H.–Y. & Sun, X. A dual–mediator for a sulfur cathode approaching theoretical capacity with low overpotential in aqueous Zn–S batteries. *Energy Environ. Sci.* **16**, 4326–4333 (2023).
3. Li, W., Wang, K. & Jiang, K. A Low Cost Aqueous Zn–S Battery Realizing Ultrahigh Energy Density. *Adv. Sci.* **7**, 2000761 (2020).
4. Yang, M. *et al.* Boosting Cathode Activity and Anode Stability of Zn–S Batteries in Aqueous Media Through Cosolvent–Catalyst Synergy. *Angew. Chem. Int. Ed.* **61**, e202212666 (2022).
5. Cui, M., Fei, J., Mo, F., Lei, H. & Huang, Y. Ultra–High–Capacity and Dendrite–Free Zinc–Sulfur Conversion Batteries Based on a Low–Cost Deep Eutectic Solvent. *ACS Appl. Mater. Interfaces* **13**, 54981–54989 (2021).
6. Mehta, S. *et al.* Unleashing Ultrahigh Capacity and Lasting Stability: Aqueous Zinc–Sulfur Batteries. *Adv. Energy Mater.* **14**, 2401515 (2024).
7. Li, H. *et al.* High–Capacity and Long–Life Aqueous Zn–SPAN Batteries with Tandem Catalysis. *Adv. Mater.* **37**, 2409771 (2025).
8. Yang, M. *et al.* Controllable Synthesis of Sub–10 nm ZnS Nanograins Confined in Micro–Size Carbon Skeleton for Aqueous Zn–S Batteries. *Adv. Funct. Mater.* **34**, 2406077 (2024).
9. Zhao, Y. *et al.* Initiating a Reversible Aqueous Zn/Sulfur Battery through a “Liquid Film”. *Adv. Mater.* **32**, 2003070 (2020).
10. Thomas, T. S., Sinha, A. P. & Mandal, D. Modulating electrolyte solvation for high–performance aqueous zinc–sulfur batteries. *J. Mater. Chem. A* **12**, 21350–21356 (2024).
11. Zhao Z. *et al.* Dual-Functional Organoiodide Additive for Highly Efficient Sulfur Redox Kinetics and Zinc Regulation in Aqueous Zinc–Sulfur Batteries. *Adv. Funct. Mater.* **35**, 2501332 (2025).
12. Liu, J., Wu, H., Ye, C. & Qiao, S.-Z. High-Entropy Sulfides Catalyze Rate-Determining Redox in Fast-Charging Aqueous Zinc–Sulfur Batteries. *Angew. Chem. Int. Ed.* **64**, e202503472 (2025).
13. Shen, S. *et al.* Improving ZnS Oxidation Kinetics Through Nucleophilic Regulation for High-Performance Zinc–Sulfur *Batteries*. *Adv. Funct. Mater.* **35**, 2420258 (2025).

14. Zhang, H. *et al.* Internal Electron Donor Accelerated Sulfur Redox for Aqueous Zn─S Batteries. *Adv. Funct. Mater.* **34**, *2406125* (2024).

15. Mehta, S. *et al.* Unlocking Long Life Aqueous Zinc-Sulfur Rechargeable Battery Derived from Zinc Waste Powering 30 LEDs. *Adv. Energy Mater.* 2501214 (2025). *DOI: 10.1002/aenm.202501214.*

16. Patel, D., Dharmesh, A., Sharma, Y., Rani, P. & Sharma A. K. Hybrid electrolyte with biomass-derived carbon host for high-performance *aqueous* Zn–S battery. *Chem. Eng. J.* **479**, 147722 (2024).

17. Zhang, H. *et al.* Redox Catalysis Promoted Activation of Sulfur Redox Chemistry for Energy-Dense Flexible Solid-State Zn–S Battery. *ACS Nano* **16**, 7344–7351 (2022).

18. Dai, P. *et al.* Spin State Modulation via Magnetic Fields in Fe Single Atom Catalysts for High-Performance Aqueous Zinc–Sulfur Batteries. *ACS Nano* **19**, 21083–21094 (2025).

19. Chang, G. *et al.* Bifunctional electrolyte additive with redox mediation and capacity contribution for sulfur cathode in aqueous Zn–S batteries. *Chem. Eng. J.* **457**, 141083 (2023).

20. Li, J., Liu, J., Xie, F., Bi, R. & Zhang, L. Synergistic Electrocatalysis and Spatial Nanoconfinement to Accelerate Sulfur Conversion Kinetics in Aqueous Zn–S Battery. *Angew. Chem. Int. Ed.* **63**, e202406126 (2024).

21. Guo, Y. *et al.* Engineering Electrolyte Network Structure for Improved Kinetics and Dendrite Suppression in Zn–S Batteries. *Angew. Chem. Int. Ed.* **64**, e202422047 (2024).

22. Guo, Y. *et al.* Hybrid Electrolyte Design for High–Performance Zinc–Sulfur Battery. *Small* **19**, 2207133 (2023).

23. Amiri, A., Sellers, R., Naraghi, M. & Polycarpou, A. A. Multifunctional Quasi–Solid–State Zinc–Sulfur Battery. *ACS Nano* **17**, 1217–1228 (2023).

24. Li, J. *et al.* Constructing a raincoat–like protective layer on sulfur cathode for aqueous Zn–S batteries. *Energy Storage Mater.* **70**, 103541 (2024).

25. Zhang, W. *et al.* Bidirectional Atomic Iron Catalysis of Sulfur Redox Conversion in High-Energy Flexible Zn–S Battery. *Adv. Funct. Mater.* **33**, 2210899 (2023).

26. Wang, M. *et al.* Simultaneous acceleration of sulfur reduction and oxidation on bifunctional electrocatalytic electrodes for quasi-solid-state Zn–S batteries. *Sci. China Chem.* **67**, 1531–1538 (2024).